3-2003

Total Dose Effects of Ionizing and Non-Ionizing Radiation on Piezoresistive Pressure Transducer Chips

Samuel J. Willmon

TOTAL DOSE EFFECTS OF IONIZING AND NON-IONIZING RADIATION

ON PIEZORESISTIVE PRESSURE TRANSDUCER CHIPS

THESIS

Samuel J. Willmon, Captain, USA

AFIT/GNE/ENP/03-11

DEPARTMENT OF THE AIR FORCE

AIR UNIVERSITY

AIR FORCE INSTITUTE OF TECHNOLOGY

Wright-Patterson Air Force Base, Ohio

AFIT/GNE/ENP/03-11

TOTAL DOSE EFFECTS OF IONIZING AND NON-IONIZING RADIATION ON
PIEZORESISTIVE PRESSURE TRANSDUCER CHIPS

THESIS

Presented to the Faculty

Graduate School of Engineering and Management

Air Force Institute of Technology

Air University

Air Education and Training Command

in Partial Fulfillment of the Requirements for the

Degree of Master of Science (Nuclear Science)

Samuel J. Willmon, BS

Captain, USA

March 2003

APPROVED FOR PUBLIC RELEASE; DISTRIBUTION UNLIMITED

TOTAL DOSE EFFECTS OF IONIZING AND NON-IONIZING RADIATION ON
PIEZORESISTIVE PRESSURE TRANSDUCER CHIPS

Samuel J. Willmon, BS
Captain, USA

Approved:

_____

James C. Petrosky, LTC, (Chairman)

10 MAR03

date

_____

David Weeks, (Member)

10 Mar 03

date

_____

Paul Kladitis, CPT, (Member)

10 MAR03

date

Acknowledgements

Table of Contents

vi

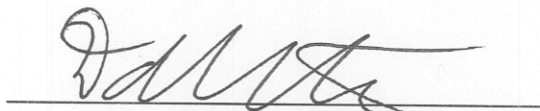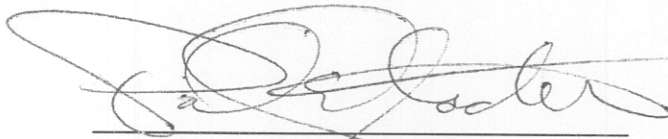# List of Figures

List of Tables

AFIT/GNE/ENP/03-11

Abstract

The effects of ionizing and non-ionizing radiation on the resistivity of silicon-based, piezoresistive bulk micro-machined chips from pressure transducers were examined. Standard current-voltage (I-V) measurements were taken in-situ and post-irradiation during isothermal annealing at room temperature. One group of chips was irradiated to a maximum total gamma dose of $1 Mrad_{Si}$ in the 11,000 Ci ^{60}Co gamma cell at Ohio State University. The second group of chips was irradiated at the Ohio State University Research Reactor facility to a maximum total neutron dose of 4 $Mrad_{Si}$ using beam port #1.

The resistivity was shown to decrease during gamma irradiation as a result of Compton current generation and increase during neutron irradiation as a result of displacement damage. During irradiation in the gamma cell, the chips exhibited a 0.45 ± 0.19 % decrease in resistivity at saturation. During the neutron and gamma irradiation in the reactor, the chips exhibited a peak change in resistivity of $2.503 \pm 0.003\%$ at 2 $Mrad_{Si}$, $3.055 \pm 0.002\%$ at 3 $Mrad_{Si}$, and 3.6921% (with unknown uncertainty) at 4 $Mrad_{Si}$. Regardless of the total dose received, all chips demonstrated a permanent change in resistivity of $0.7697 \pm 0.0006\%$ at room temperature.

I. Introduction

Background

This research examines the relationship between the total radiation dose from ionizing and non-ionizing radiation and the resistivity of a piezoresistive chip in an effort to determine the contributions of ionizing and non-ionizing irradiation to piezoresistive transducer failure. For application purposes, this research specifically examines the behavior of silicon chips as fabricated for use in the Ametek IPTG-0600DSFS model transducer.

This research stems from problems encountered at the Los Alamos National Laboratory (LANL), New Mexico, related to the stockpile stewardship program. In essence, an experiment at LANL requires that the internal pressure of a containment vessel be taken while the components are irradiated using the annular core research reactor (ACRR) at Sandia, New Mexico. This provides the researchers at LANL a great degree of confidence that no possible contaminants have leaked from the vessel. In addition, further tests will require pressure and acceleration measurements as a shock wave is propagated through a similar vessel. To this end, the researchers at LANL have incorporated a piezoresistive pressure transducer into their test design.

Thus far, the researchers at LANL, in collaboration with Arizona State University, have made several observations concerning their piezoresistive pressure transducers. They have observed that several models fail initialization tests after sitting in a storage vault where an estimated gamma flux exists of 10^5 cm^{-2} s^{-1}; some models fail single reactor pulses (20-30 MW$_{th}$, with an estimated pulse width of 10ms); and some models survive multiple reactor pulses. Further investigations at Arizona State University have

tested the functionality of piezoresistive pressure transducers while irradiated in a gamma cell and similar results were discovered.[1]

Several factors exist which complicate the interpretation of the studies performed thus far. To date, no solid dosimetry tests have been performed to determine the actual dose delivered to the piezoresistive pressure transducers in either the storage vault or the ACRR at Sandia. In each test, the transducers were incorporated "as fabricated" and no investigations into the design and inner structure of the transducers have been performed.

With sponsorship from the Defense Threat Reduction Agency, Washington D.C., this research serves as an initial investigation into the behavior and performance of piezoresistive pressure transducers in radiation environments.

Problem Statement

The goals of this thesis are: (1) to characterize the relationship between total dose and resistivity across the piezoresistive chip's Wheatstone bridge, (2) identify the chip's radiation dose limits, (3) characterize the recovery profile as a function of operating voltage and temperature, and (4) to investigate possible annealing conditions which allow the devices to recover post-irradiation.

Scope

This research investigates the change in resistivity across a piezoresistive silicon chip fabricated for use in a pressure transducer while irradiated. Two sources of radiation are used in this research: a ^{60}Co gamma cell (providing ionizing radiation only) at the Ohio State University (OSU) reactor facility, and a research reactor (providing ionizing

2

and non-ionizing radiation, also at OSU). In-situ I-V measurements are taken during

irradiation and during an annealing period (at room temperature).

General Approach

The approach to this research follows a "simple" theory-model-experiment cycle.

After developing the theory outlining the effects of radiation on silicon, a model is

presented which serves to predict the expected behavior following irradiation, then the

experiment confirms or denies the hypothesis presented by the model. Based on the

outcome of the experiment, the theory may require refinement in order to justify altering

the proposed model.

Following a comprehensive, open-source literature search, several initial findings

were evident. No current work exists examining the effect of radiation on piezoresistive

materials.   Numerical modeling and analysis is outside the scope of and time available

for this research. Many studies have been performed on the radiation effects on silicon

crystals and electronic components. An initial investigation into the design and structure

of the Ametek transducer identified several points of failure. Based on these findings, the

focus of this research is narrowed to the effect of radiation on the piezoresistive chip.

That no current studies have explored the influence of radiation on the behavior of

piezoresistive materials stems most likely from the nature of radiation environments. The

Institute of Electrical and Electronics Engineers (IEEE) categorizes radiation

environments as the following: the space environment, the nuclear reactor environment,

and the nuclear weapon (following detonation) environment. None of these

environments explicitly calls for the use of a piezoresistive pressure sensor. In the case

of a nuclear reactor, for example, it is more sound to not employ a transducer in the radiation environment than to attempt to monitor the coolant pressure via a transducer near the reactor's core.

Previous work in the area of radiation effects on electronic devices is relied upon in order to extrapolate the effect of the radiation on the entire transducer. In addition, the radiation sources used in this research at OSU fit a long duration, square pulse and the reactor pulses used by the LANL researchers at the ACRR in Sandia fit a narrow, short pulse. Due to the differing pulse shapes, the results of this research are further extrapolated to predict the behavior of the piezoresistive chip following a pulse of radiation from the ACRR in Sandia.

II.   Background

This chapter develops the theory regarding the piezoresistive effect and demonstrates the construct of piezoresistive pressure transducers. In addition, the model used in this research and the effects of radiation on semiconductors is presented.

Piezoresistive Effect

The first published documents outlining the nature of the piezoresistance effect appear in the 1930's. The work of the Curie brothers in 1880 (who are credited with discovering the piezoelectric effect) and Woldemar Voigt, who in 1928 published *Lehrbuch der Kristallphsyik,* made great strides in relating the properties of crystals to their geometric symmetry.   Professor Bridgman at Harvard University was the first to study the effects of a mechanical stress on the electrical resistance of crystals.[2] Assuming Ohm's law holds, Bridgman first expresses the electric field vector , E, as a function of the current vector:

$$\vec{E} = r\,\vec{J} \tag{1}$$

where E is the potential gradient vector, q is the current vector, and r is the matrix of coefficients which satisfy the equation. Bridgman asserts that if a mechanical stress is applied to the crystal, the matrix of coefficients will change according to the following form:

$$\delta r_{i,j} = \begin{pmatrix} \delta r_{1,1} & \delta r_{1,2} & \delta r_{1,3} \\ \delta r_{1,2} & \delta r_{2,2} & \delta r_{3,2} \\ \delta r_{1,3} & \delta r_{3,2} & \delta r_{3,3} \end{pmatrix} \tag{2}$$

Research examining the piezoelectric effect prior to the 1950's focused primarily on identifying materials with piezoelectric properties. Once silicon had been identified as having piezoelectric properties, researchers focused on identifying silicon's piezoresistive coefficients. These measurements allowed for the identification of the relationship between the induced electric field caused by an applied stress or strain (and conversely, the displacement caused by an applied electric field).[3] It was not until nearly a quarter of a century later that Charles Smith of the Bell Laboratories in New Jersey described the piezoresistive effect in silicon and provided the complete tensor that characterizes the piezoresistive coefficients.[4] Smith continued Bridgman's formulation by expressing the change in the electric field in terms of equation (2):

$$\overrightarrow{\delta E} = \delta\rho \cdot \vec{J} \tag{3}$$

where Smith has re-defined the matrix of coefficients as d?. For convenience, Smith divides both sides by the scalar resistivity (?) resulting in:

$$\frac{\overrightarrow{\delta E}}{\rho} = \Delta \vec{J} \tag{4}$$

where ? is defined as ? = $(d?_{i,j})$/?. Smith further defines ? in terms of the applied stress X as:

$$\Delta = \Pi X \tag{5}$$

where ? is the matrix of piezoresistance coefficients and X is the matrix that describes the applied stress. Given a constant current, equation (4) can be written in terms of the piezoresistance coefficients and the applied stress:

6

$$\frac{\overrightarrow{\delta E}}{\rho} = \Delta X \, \vec{J} \qquad\qquad (6)$$

While Bridgman took a mathematical approach to describing the piezoresistance effect, Smith made the additional step (in conjunction with C. Herring, also of Bell Laboratories) in attempting to develop the theory explaining why the piezoresistance effect occurs. To accomplish this, Smith employed the "many valley" lattice model. According to this model, electron equipotential regions appear as ellipsoids along the coordinate axes. In an unstressed crystal, these regions are symmetrical and of equal size as the electrons have no preferred location. As shown in Figure 1, a stress that is applied to the crystal (here in the [1,0,0] direction), gives rise to a change in the equipotential regions and electrons are "transferred" in a preferred direction.
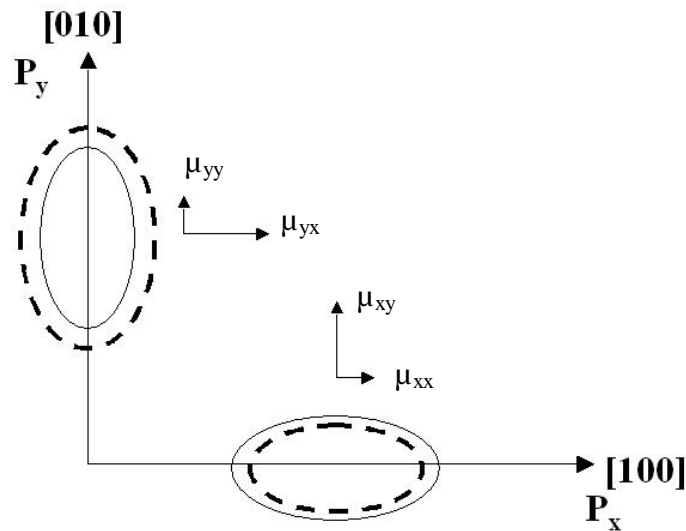
Figure 1: "Many-valley" model equipotential surfaces

Smith asserts that this equipotential surface change results in a change in the lattice mobility. In Figure 1, the direction and magnitude of the arrows associated with the mobility indicate the change in mobility, μ. The dashed lines indicate the changes in the equipotential surfaces.

In applying his theory, Smith discovered that in some cases his predicted values for the piezoresistance coefficients did not agree with work previously done by Bridgman. With assistance from Herring, Smith indicates that other electron transfer mechanisms must exist. Smith postulated that a strain on a crystal produces "change in resistance through its action on the phonons, on the electrons, and on the coupling between them."[4]

Further refinement of Smith's theory on the piezoresistance effect has not been accomplished. Although one can apply the Hamiltonian and other many-bodied physics concepts to a crystalline lattice, solving these systems of equations in terms of electron and phonon interactions requires complete knowledge (in time, position, and energy) of the nuclei, electrons, and phonons.[5] Even with the supercomputing capability available today, this task is daunting. As a result, Smith's theory is generally accepted. While Smith's theory does not provide a means to calculate piezoresistance coefficients explicitly, piezoresistance measurements can be made and the theory applied accordingly.

Pressure Transducers

The fundamental goal of any transducer is to transform a given physical parameter (force, mass, velocity, etc.) into an electric signal. Duane Tandeske offers several parameters that can be used to determine the type of transducer appropriate for a given situation. The most common parameters being "range, accuracy, size and price."[6]

Piezoresistive pressure transducers capitalize on all four of the selection parameters given.

In the typical piezoresistive transducer, four resistors are arranged in a Wheatstone bridge. In order to account for the resistance changes due to temperature, temperature-compensating resistors are often included in the circuit. Figure 2 shows a general-purpose Wheatstone bridge.
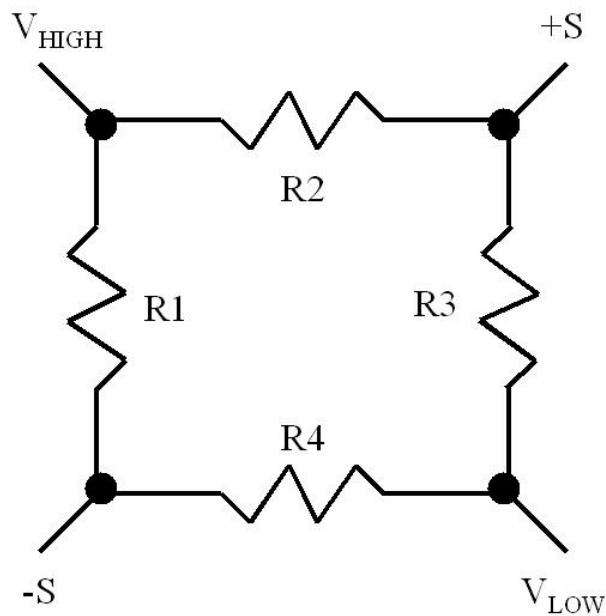
Figure 2: General-purpose wheatstone bridge

The Wheatstone bridge as shown in Figure 2 is fabricated on a thin chip of silicon where the expected pressure is applied to the center of the bulk micro-machined silicon chip. A common technique is to create the resistive circuit path (a p-channel) by ion implanting boron into an n-type silicon substrate. In order to minimize leakage, the substrate is reverse-biased, which creates a depletion region at the pn-junction.

The four resistors of the Wheatstone bridge are fabricated as strain gages and the resulting circuit is shown in Figure 3. A pressure applied to the center of the chip creates stress lines within the crystal. The location of the piezoresistive strain gages capitalizes on the locations of the maximum induced strain. A schematic depicting the stress lines created is shown in Figure 4. When taken together, the simple logic behind the piezoresistive pressure transducer is apparent.

Wheatstone bridge resistors
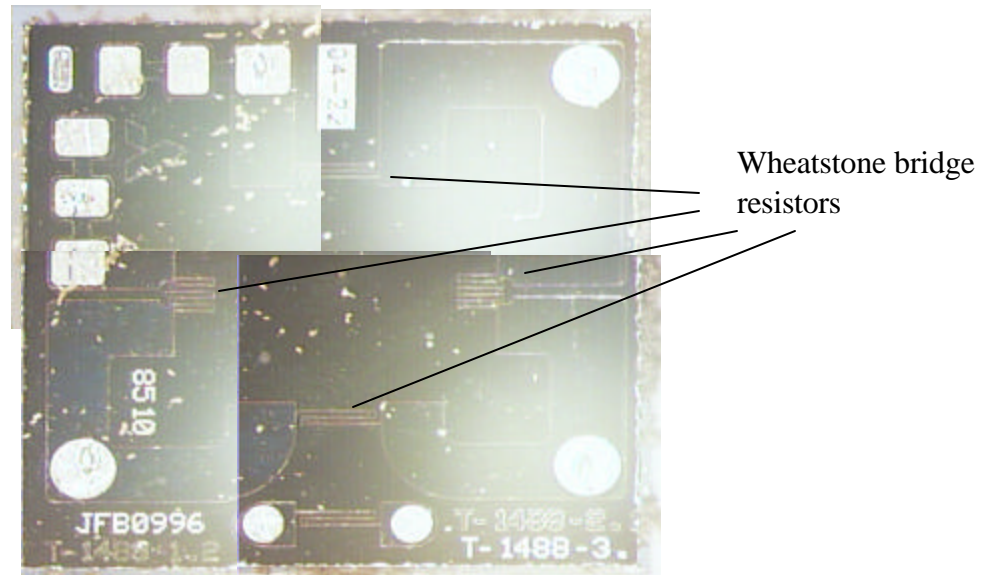
Figure 3: Ametek Piezoresistive Chip

Maximum stress at the edges
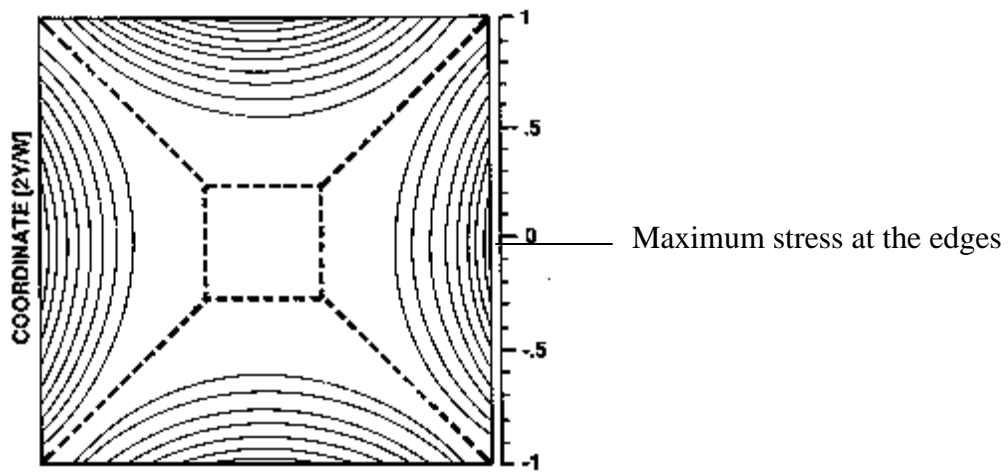
Figure 4: Contour Plot of Stress lines[6]

Electrical and Mechanical Properties of Silicon

Because of its semi-conducting properties, the relatively high level of the

development in the manufacturing processes involved in generating ultra-pure silicon,

and its high piezoelectric coefficients, silicon-based piezoelectric devices remain at the

core of current technological development. Silicon's tensile and compressive strengths

are greater than steel and it has an ability to sustain a greater number of cycles of tension

and compression than steel. These physical properties combined with its semi-

conducting properties make single-crystal silicon an excellent material for a transducer.[7]

Table 1 lists several fundamental properties of silicon.

A wide range of silicon based micro-electromechanical systems (MEMS)

employed in terrestrial applications currently exists. The low weight, cost, and power

requirements of MEMS devices combined with the ability to achieve cost effective

redundancy make them ideal for space applications as well.[8] The continued development

of space technology and the need to collect data in radiation environments on earth

requires the design of sensors capable of surviving expected radiation dose levels.

Table 1: Fundamental Properties of Silicon[9]

Property	Value
Band gap (300K)	1.12 eV
Electron Mobility (300K)	1500 (cm^2 V^{-1} s^{-1})
Hole Mobility (300K)	450 (cm^2 V^{-1} s^{-1})
Ionization Density[10]	4.3×10^{13} (cm^{-3} rad^{-1})
Intrinsic Resistivity	2.3×10^5 (O-cm)
Carrier lifetime	10^{-6} (s)

Semiconductor Modeling

Several modeling tools exist in order to examine the behavior of semiconductors.

This research incorporated PISCES-II (version 9009-Win32 x86) modeling in order to

obtain benchmarks for the current measurements obtained. In essence, the PISCES-II code solves charge carrier transport equations and Poisson's equation in two dimensions.[11] Given a physical description of the semiconductor (material, length and width, as well as dopant type and concentration), the location of electrodes, and the applied potential, PISCES-II calculates the current at the electrodes.

The two electrical paths from V_{HIGH} to V_{LOW} in Figure 2 can be represented as two rods of p-type silicon with electrodes placed on the faces of both ends (shown in Figure 5). Using the outer dimensions of the chip as a reference, the channel width (W) and length (L) were measured from the enlarged photograph of the chip in Figure 3 (4.7 ±0.01 µm and 5.618 ± 0.001 mm, respectively). The depth (D) of the channel of 10 ± 1 µm was estimated from current literature on piezoresistive fabrication techniques.
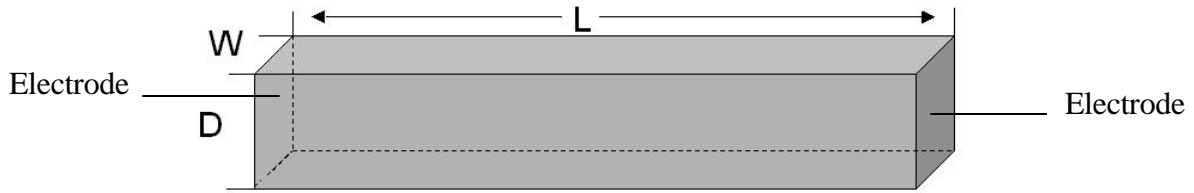
Figure 5: P-channel model

The resistivity of the p-type silicon is given by the following equation[12]:

$$\rho = \frac{R(2A)}{L} \qquad (7)$$

where the area (A) has been multiplied by two in order to account for both conducting channels. Initial resistance measurements of the p-channels resulted in an average

resistance (R) of 9.7 ± 0.1 kO.   Equation (7) results in a calculated resistivity of $0.016 \pm$ 0.002 O-cm.

There are many references on semiconductor materials that show the relationship between the dopant concentration and the resistivity in silicon. Using one such figure in Van Lint's book *Mechanisms of Radiation Effects in Electronic Materials (Vol. 1)*[10], the dopant concentration of the Ametek p-channel is approximately 10^{19} cm-3. The physical parameters, the estimated dopant concentration, the placement of the electrodes, and the carrier lifetimes given in Table 1 provide all of the necessary information required by PISCES-II to solve the *continuity equations* and Poisson's equation.

The *continuity equations* describe the transport of charge carriers in semiconductors as function of position and time.[13] In one dimension, the continuity equations are:

$$\frac{d}{dt}p = \frac{-1}{q}\left(\frac{d}{dx}J_p\right) - U_p(x,t) + G(x,t) \tag{8}$$

$$\frac{d}{dt}n = \frac{-1}{q}\left(\frac{d}{dx}J_n\right) - U_n(x,t) + G(x,t) \tag{9}$$

where $J_{p,n}$ are the hole and electron currents, p and n are the carrier densities, q is the fundamental unit of charge, and U and G are the recombination and generation rate densities, respectively. The following equations express the hole and electron currents in terms of the electric field and their respective diffusion coefficients[13]:

$$J_p = q\mu_p pE - qD_p\left(\frac{d}{dx}p\right) \tag{10}$$

13

$$J_n = q\mu_n nE - qD_n\left(\frac{d}{dx}n\right) \tag{11}$$

where $\mu_{p,n}$ are the carrier mobilities, $D_{p,n}$ are the carrier diffusion coefficients, and E is the electric field. The diffusion coefficients are related to the diffusion length and carrier lifetime via the following equation[10]:

$$L_n = \sqrt{D_n\tau_n} \tag{12}$$

The diffusion coefficients are also related to the carrier mobility and the temperature through Einstein's relation[10] (written here for electrons):

$$D_n = \mu_n\left(\frac{kT}{q}\right) \tag{13}$$

where k is Boltzman's constant, and T is the temperature [K].

"Poisson's relates the electric field distribution to mobile charge and active impurity densities:"[13]

$$\frac{d}{dx}E = \frac{q}{\varepsilon}(p - n + N) \tag{14}$$

where e is the permittivity of the material, and N is the dopant concentration.

The modeling effort was limited due to the inability of PISCES-II to include the effects of ionizing and non-ionizing radiation directly. Despite this limitation, the results from the PISCES-II model were expected to favorably compare to baseline tests performed on the chips prior to irradiation. The modeling results then indicate the lower limit on the in-situ measurements during irradiation.

Radiation Effects on Semiconductors

Despite an exponential growth in the application of silicon technology, researchers have devoted little effort toward investigating the effects of radiation on piezoresistive devices. Volumes, however, have been written describing theories regarding the radiation damage mechanisms in bulk silicon. These studies have characterized the changes in carrier concentration, mobility, and lifetime as a function of total dose in silicon.[14]

Matthias Werner and Wolfgang Fahrner (ranking members of IEEE) call for increased studies of MEMS devices in "harsh" environments. However, their paper focuses on the influences of temperature on device performance and discounts the application of Si-Si devices due to silicon's small band gap.[15] Knudson (et al) investigated the effects of radiation on MEMS accelerometers through proton and heavy ion bombardment. Their conclusions, however, fall short of identifying the relationship between the postulated damage mechanisms and the resistivity of the sensor material.[16]

Swarupa Padgaonkar (et al) employed a 14 MeV neutron generator in his 1990 research into the effects of high energy neutrons on the Hall mobility, carrier concentration, energy levels of defect sites, and the minority carrier lifetime in phosphorus doped silicon. Padgaonkar found that the energy levels of the defect sites were identical in both cases. Padgaonkar also found that high-energy neutron irradiation resulted in a degradation in mobility.[17]

C. I. Lee (et al) conducted research into the effects of radiation on MEMS accelerometers and was able to identify a difference between entire sensor irradiation and

sensing element only irradiation. Their research, however, failed to characterize the decline in sensor function as a result of the dose received or its recovery profile.[18]

The principle source of ionizing radiation damage stems from Compton scattering.[19] Incident gamma rays that elastically scatter off of atomic electrons produce Compton electrons. While electrons with sufficient energy to displace silicon atoms within the lattice can create vacancy-interstitial pairs, the probability for scattering is much greater than the probability of generating vacancy-interstitial pairs.   The electrons generated can also scatter and produce additional ionized electrons, recombine with holes, occupy trap sites, or exit the device as unwanted current (photocurrent). In the literature, the creation of ionized electrons (which leave behind holes) is often referred to as *carrier injection*. In terms of the quantity of electron-hole pairs created, Low Level Injection (LLI) occurs when fewer carriers are injected per unit volume than original carrier concentration. Alternatively, High Level Injection (HLI) occurs when more carriers are injected per unit volume than the original carrier concentration.[20]

Messenger states that due to silicon's low displacement cross section ($3x10^{-24}$ cm^2) and the range of neutrons in silicon (on the order to centimeters), incident neutrons will produce uniformly distributed collision sites throughout the crystal and most likely leave the crystal following a single collision. When a neutron with sufficient energy collides with an atom, it will displace the atom from the crystal lattice. The displacement threshold energy is 20 eV for silicon. The displaced atom (also referred to as a primary knock on atom, PKA) will lose its energy through ionizing and non-ionizing interactions and come to rest in an energetically favorable location with the lattice. The PKA leaves behind a track of vacancy-interstitial pairs until it no longer has enough energy to

displace any more atoms. This final location, however, need not be in a location that follows the pattern of the crystal structure. The interstitials leave behind a lattice vacancy. Because the majority of the vacancy-interstitial pairs lie within a few atomic spacings of each other, they recombine with a high probability. Messenger states that this accounts for nearly an annealing of 95% of the vacancy-interstitial pairs produced in this fashion. While interstitials do not form electrically active defect sites, vacancies serve as trapping and recombination centers and reduce the carrier mobility, density, and minority carrier lifetime.[14] Additionally, research has shown that vacancies are mobile in p-type silicon at temperatures above 160K.[21]

Defect Effects and Annealing

"The words *anneal* and *annealing* refer to the partial or total self-healing of an electronic component or system after exposure to damaging nuclear radiation."[20] The annealing process in a crystal is highly temperature and time dependent. As temperature increases, the thermal energy imparted to defects within the lattice gives them sufficient energy to become mobile. In this manner, vacancies and interstitials may recombine. It is also possible, however, for defect atoms within the lattice structure to form stable associations with existing impurities and further degrade device performance.[20] The longer the device is allowed to anneal at a temperature at which defects are mobile, the more defects that will anneal. Generally, the annealing process takes the form of a decaying exponential.

Following the generation of defect centers within the bandgap, several possible effects may occur. The primary effects of defect centers are electron-hole pair

17

generation, recombination, trapping, compensation, and tunneling (the first four of which are depicted in Figure 6: Effects of Defect Centers within the Bandgap).[22]
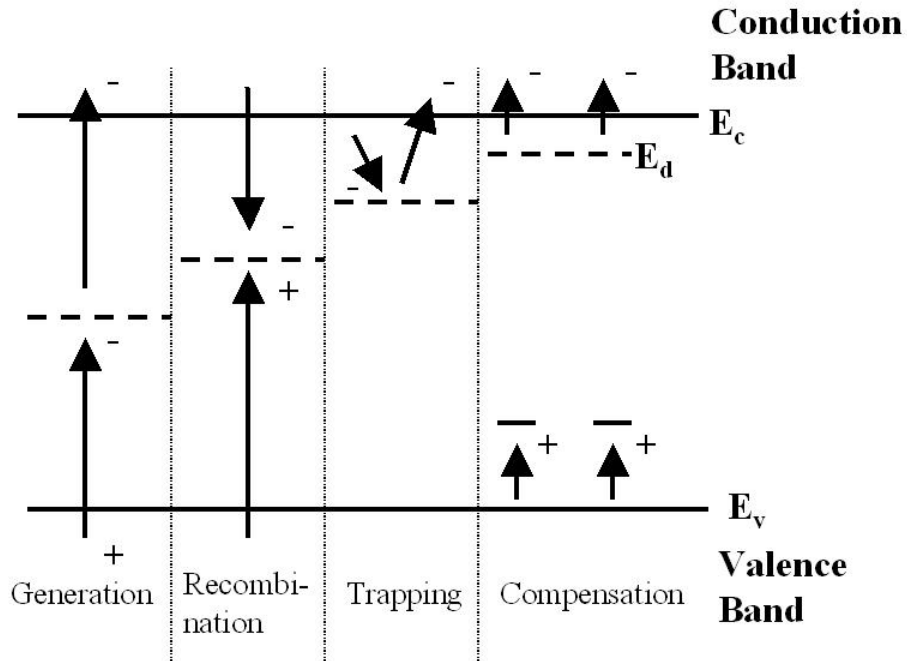
Figure 6: Effects of Defect Centers within the Bandgap

A valence band electron may gain sufficient thermal energy to become excited to the defect center. Further thermal excitation may allow the electron to jump to the conduction band. Defect centers located near the mid-gap region contribute the most to electron-hole pair generation.

Recombination occurs when a defect center captures a charge carrier and then captures another of the opposite sign. The average amount of time a charge carrier spends within the bandgap is referred to as the recombination lifetime.

Charge carriers may also become temporarily trapped in a shallow level defect. Once trapped, the charge carrier is later released back to its energy band.

18

Defects may also compensate for donors or acceptors, depending on their charge state and location within the bandgap. In this manner, deep lying acceptor-type defects compensate for donor free electrons. This results in the decrease in the carrier concentration.

Development of Damage Coefficients

As described above, the primary radiation effects observed in semiconductors are a change in carrier mobility, carrier density, carrier lifetime, and the generation of a photocurrent. In order to predict how these parameters will change following irradiation, damage coefficients have been developed which describe the impact of the radiation on each parameter.[10] The minority carrier lifetime following irradiation is given by:

$$\frac{1}{\tau} = \frac{1}{\tau_o} + K_\tau \cdot \Phi \tag{15}$$

where t is the minority carrier lifetime following irradiation, t_o is the minority carrier lifetime prior to irradiation, K_t is the lifetime damage coefficient, and F is the radiation fluence. Similarly, the mobility following irradiation is given by:

$$\frac{1}{\mu} = \frac{1}{\mu_{Lo}} + \frac{1}{\mu_{Io}} + K_\mu \cdot \Phi \tag{16}$$

where μ is the mobility following irradiation, μ_{Lo} is the lattice mobility prior to irradiation, μ_{Io} is the impurity scattering mobility prior to irradiation, K_μ is the mobility damage coefficient. And the electron concentration following irradiation is given by:

$$n = n_o - K_n \cdot \Phi \tag{17}$$

where n is the electron density following irradiation, n_0 is the electron density prior to irradiation, K_n is the carrier concentration damage coefficient. K_n can also be thought of as the carrier removal rate. All of the damage coefficients presented in equations (15) through (17) are functions of the "Fermi level, temperature, and irradiation composition."[10]

As shown in Figure 7, the radiation damage mechanisms described above become important only once the neutron fluence rises above distinct threshold values. While the graph specifically described the impact of neutron fluence on the damage mechanisms for n-type silicon with a resistivity of 2 ohm-cm, the information contained in the figure applies to the p-type silicon used in this research as well.
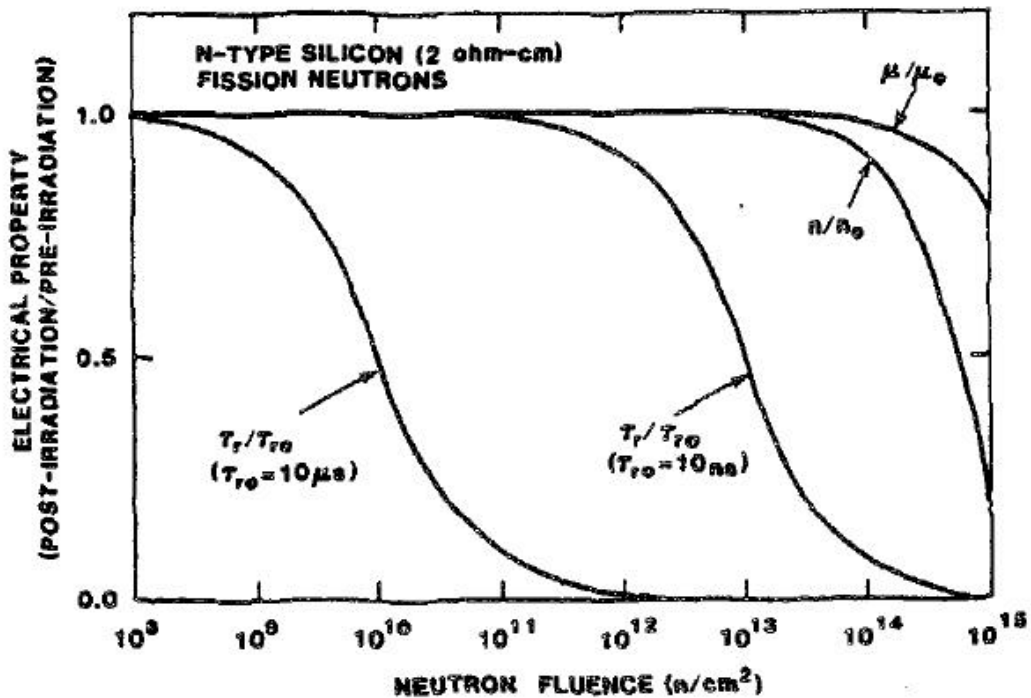
Figure 7: Mechanism Importance as a Function of Neutron Fluence[22]

Change in Resistivity as a Function of Total Dose

With electrical resistivity is defined as the inverse of conductivity, the change in resistivity is given by the following equation:

$$\delta\rho = \frac{1}{e_o\left(\delta n\mu_n + \delta p\mu_p\right)} \tag{18}$$

where e_o is the fundamental unit of charge, dn is the excess electron density, dp is the excess hole density, and the μ-terms are their respective mobilities.

In the case of ionizing radiation, the primary effect is observed as an excess of minority charge carriers. In p-type silicon, where the electrons are the minority charge carrier, the addition of holes through ionization is negligible compared to the initial density of holes, therefore, equation (18) reduces to:

$$\delta\rho = \frac{1}{e_o\left(\delta n\mu_n\right)} \tag{19}$$

By re-arranging equation (17) and substituting the change in the number of charge carriers as a function of radiation fluence, a negative change in resistance is predicted:

$$\delta\rho = \frac{-1}{e_o\left(K_n\cdot\Phi\mu_n\right)} \tag{20}$$

As shown in Figure 7, however, neutron irradiation at high fluence levels affects all three of the carrier parameters. Enough information is not gained from current measurements to explicitly solve the Poisson and carrier current equations given in the preceding section. Information concerning the behavior of the resulting change in resistivity can be deduced from the damage coefficient relations.

21

Based on the form of equation (15), carrier lifetimes will decrease as the fluence increases. Similarly, from equation (16) it is evident that the mobility will increase as the fluence increases. And as seen in the case of ionizing radiation, the number of excess charge carriers decreases proportionally with the increase in fluence.

III.   Experiment

The experimental procedure used in this research consists of the measurement system design and characterization, chip preparation and characterization, gamma cell irradiation, reactor irradiation, and finally data analysis. This research utilized the piezoresistive chips from the Ametek IPTG-600 integrated pressure transducer.

Experimental Procedure

From the problem statement, the primary goal of this research is to determine the effect of ionizing and non-ionizing radiation in piezoresistive silicon chips. Because the reactor environment consists of both gammas and neutrons, the contribution of the photocurrent generated must be accounted for in the in-situ measurements. In order to determine the magnitude of the photocurrent generated during irradiation in the reactor, the gamma cell at Ohio State University (OSU) was used.

Time at both the gamma cell facility and the reactor at OSU and budget served as the primary constraints during the development of the experimental procedure. In order to achieve the goal of obtaining statistically significant results, four devices were obtained from Ametek for the gamma cell irradiation and additional four devices for the reactor irradiation tests. In order to maximize the time available, a step-wise total dose irradiation scheme was developed. As shown in Figure 8, the irradiation scheme starts with all four devices being irradiated simultaneously. This allows for a sample size during the first irradiation cycle of four. As each 25% interval of the total dose is reached, one device is removed. Clearly, any results from the final irradiation cycle with a sample size of one are suspect.
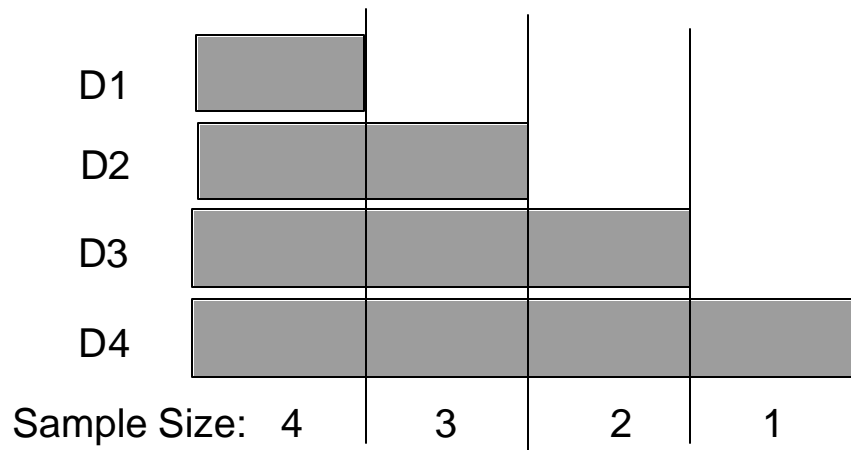
Figure 8: Irradiation scheme

Measurement System Design

A Keithley-237 Signal Measurement Unit, SMU, served as the primary measurement unit and focal point of the measurement system. The SMU allows the user to set operating parameters and collect data using via a GPIB card. As the SMU does not have the ability to provide a voltage or current source to multiple independent devices, a control box is needed. In order to provide in-situ measurements during irradiation and during annealing, test mounts are needed for the gamma cell, the beam port, and an annealing station. Figure 9 shows a schematic of the measurement system design.
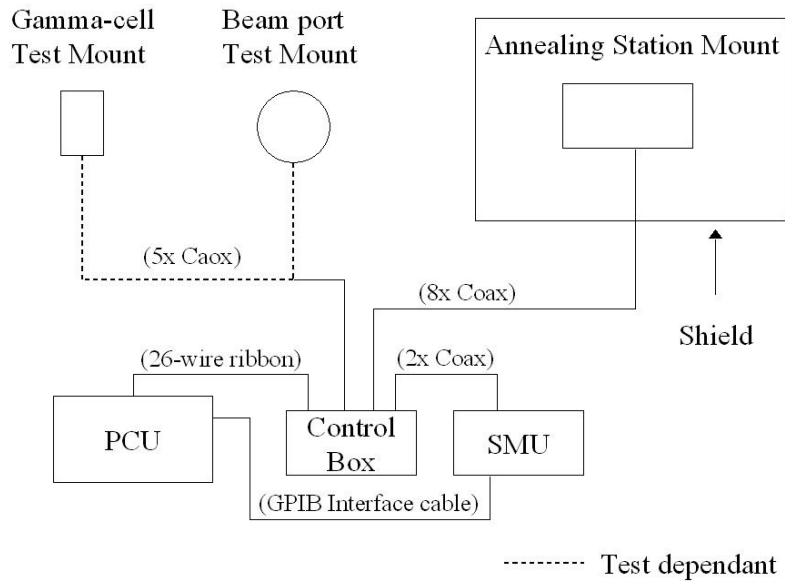
Figure 9: Measurement system design

In order to reduce the leakage current contribution to the measurements, eight 4N37 optoisolators were used to serve as switches in the control box (see Figure 10 and 9). The optoisolators consist of an LED connected to a transistor via a *light pipe*. The LED and the transistor are isolated from external light sources by the packaging material.

By connecting the transistor side of the optoisolators in parallel to the output-high terminal on the SMU, current could pass through only one piezoresistive chip at a time. The eight output pins of the parallel port on the CPU were individually wired to the optoisolator LED inputs. Sending the correct binary bit to the parallel port turned on a specific optoisolator. Standard LEDs mounted onto the control box allowed the user to follow system operations. Twelve coaxial cable connectors were connected to the eight optoisolator emitter terminals in order to provide connectivity with radiation stations one through four, and annealing stations one through eight. Radiation stations one through four were controlled by the same optoisolators as the annealing stations one through four.

25
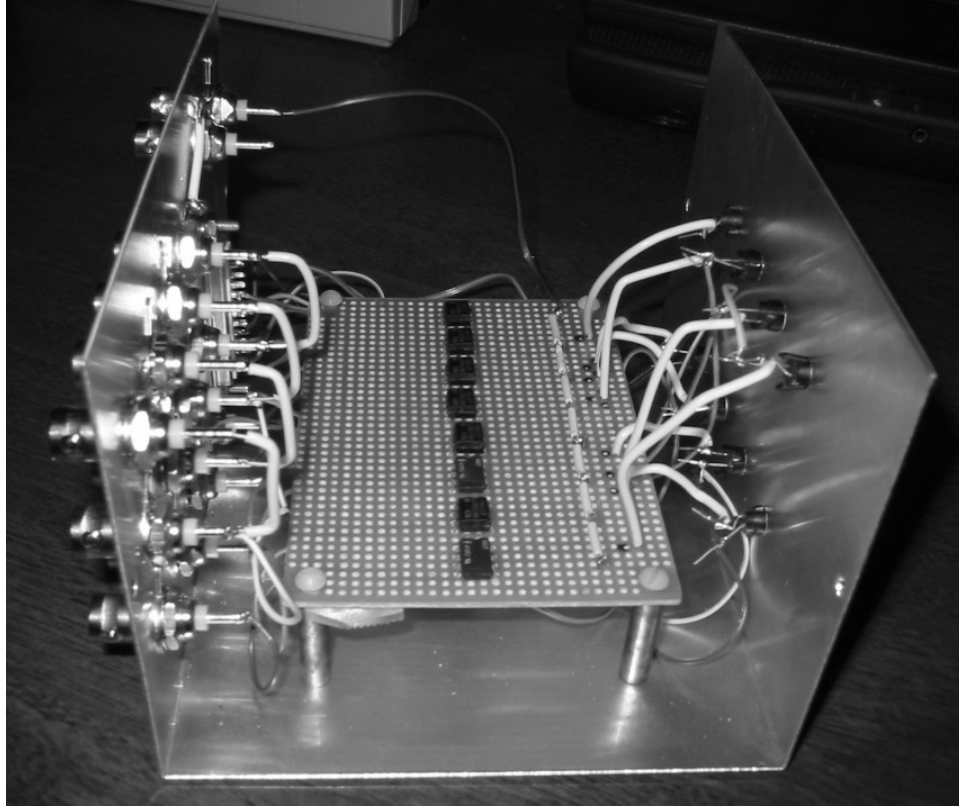
Figure 10: Measurement System Control Box (side view)

Figure 11: Measurement System Control Box (rear view)

Two irradiation stations were designed – one for the gamma cell irradiation, one for the reactor irradiation. An additional station was designed to perform measurements during annealing. The gamma irradiation station was constructed from a 1mm thick aluminum hobby box in order to ensure that charged particle equilibrium was maintained during irradiation in the gamma cell. A 124-pin socket soldered to a breadboard mounted inside of the hobby box allowed the dip-mounted chips to be slipped into designated sockets. Similarly, the beam port irradiation station was constructed from four inch long, 5-inch diameter PVC tube with the chip sockets mounted a Plexiglass plate attached to one end. A thin Plexiglas plate mounted in the center of the tube was fitted with coaxial cable connectors. A final Plexiglass plate mounted on the rear of the station was fitted with a threaded Plexiglass rod that allowed the entire station to be screwed onto the end of a paraffin plug. This arrangement provided additional radiation shielding by preventing radiation from streaming out of the beam port. Similar to the gamma cell station, the annealing station (see Figure 12) was constructed from an aluminum hobby box with eight coaxial connectors to provide connectivity with the main control box.
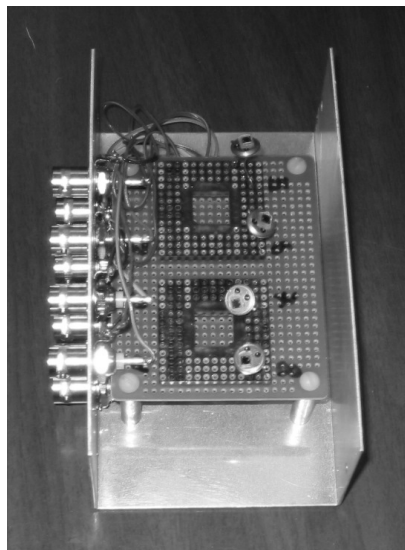
Figure 12: Annealing Station (top view)

A type-K thermocouple was used during the beam port irradiation runs in order to monitor the temperature inside the beam port at the chips' location. The junction between thermocouple cable and coaxial cable was immersed in liquid nitrogen to move the reference junction temperature away from room temperature. An exponential fit to the type-K thermocouple data chart allowed the test control program to convert the measured voltage directly into a temperature reading. Thermocouple accuracy in the temperature range near 300K (room temperature) is $\pm 2.2\ ^{\circ}$C. When used, the thermocouple was connected to the control box at annealing station eight.

A Visual Basic program, written as a user interface, controlled all operations performed by the measurement system. The program performed connectivity checks, system warm up procedures, controlled measurement cycle sequencing, established operating parameters for the SMU, controlled the optoisolators, logged data, and maintained operational system log.

Measurement System Characterization

Once completed with the measurement system design, a series of tests were performed in order to determine the effectiveness of the measurement system. Principle operating parameters of the measurement system are the optoisolator leakage currents and the maximum passable currents. In order to identify these two parameters, the optoisolators were tested in their *on* and *off* states.

In order to test the on-state condition, the transistor output current was measured as a function of applied voltage to the transistor input. The on-state current measurements (as shown in Figure 13), indicate a degree of variability in the maximum passable current between the optoisolators. While the optoisolators may serve as variable

resistors, with an expected p-channel current of 10μA (from V=IR) with an applied

voltage of one volt, it is clear that none of the optoisolators limit the expected current.

Statistical analysis of the results from the on-state measurements shows that the average

relative error in the measurements of the optoisolators is less than 0.3%.
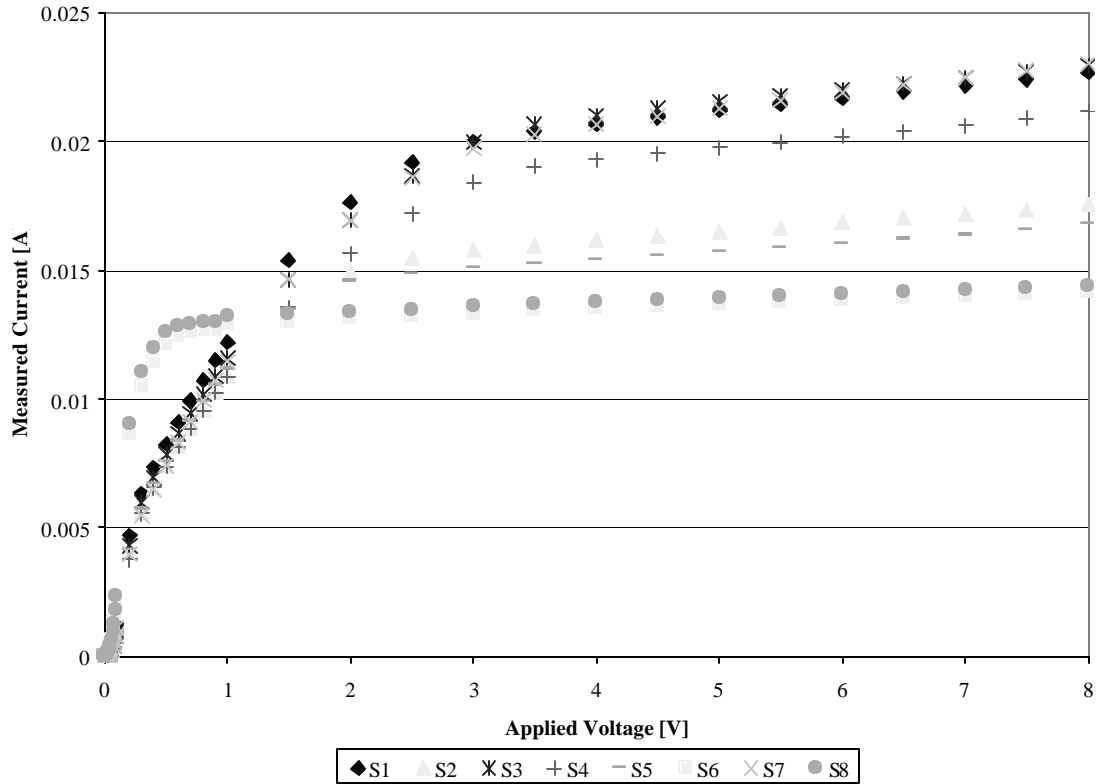
Figure 13: Optoisolator on-state

In order to test the off-state condition, the transistor output current was again

measured as a function of applied voltage to the transistor input. This time, the

optoisolators were disconnected from the CPU in order to disrupt the power to the LEDs.

As shown in Figure 14, the results from the off-state condition tests indicate that the

maximum contribution to system measurements owing to leakage from the optoisolators

is on the order of 10nA. Statistical analysis of the results of the off-state measurements

shows that the relative standard deviation does not fall below 10% unless the measured signal is above 25nA.
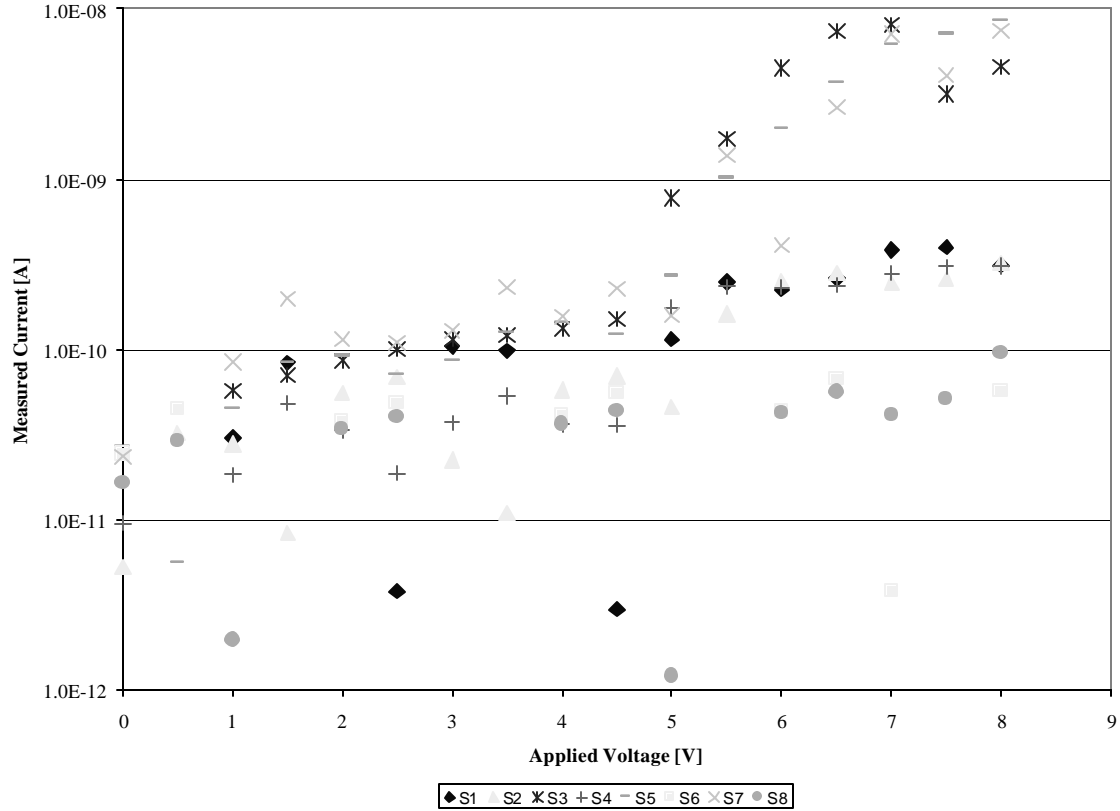
Figure 14: Optoisolator off-state

Following the on- and off-state condition tests, a standard 10kO (±10%) resistor was used to bench-test the measurement system. In order to test the system without including the optoisolators, the resistor was hard wired to the control box at the SMU terminals using jump cables. As shown in Figure 15, system noise does not impact the current measurements at voltages above 2mA (labeled as "error threshold").

Figure 15: Standard resistor bench test (without switches)

The second bench test of the measurement system included the optoisolators. For this test, the 10kO resistor was hard wired to the optoisolator output terminal, one at a time, and jumped to the SMU input terminal. The results of this test show that the calculated resistance, which should fall within 10% of 10kO, does not meet the specified tolerance until the applied voltage is greater than 0.1V.
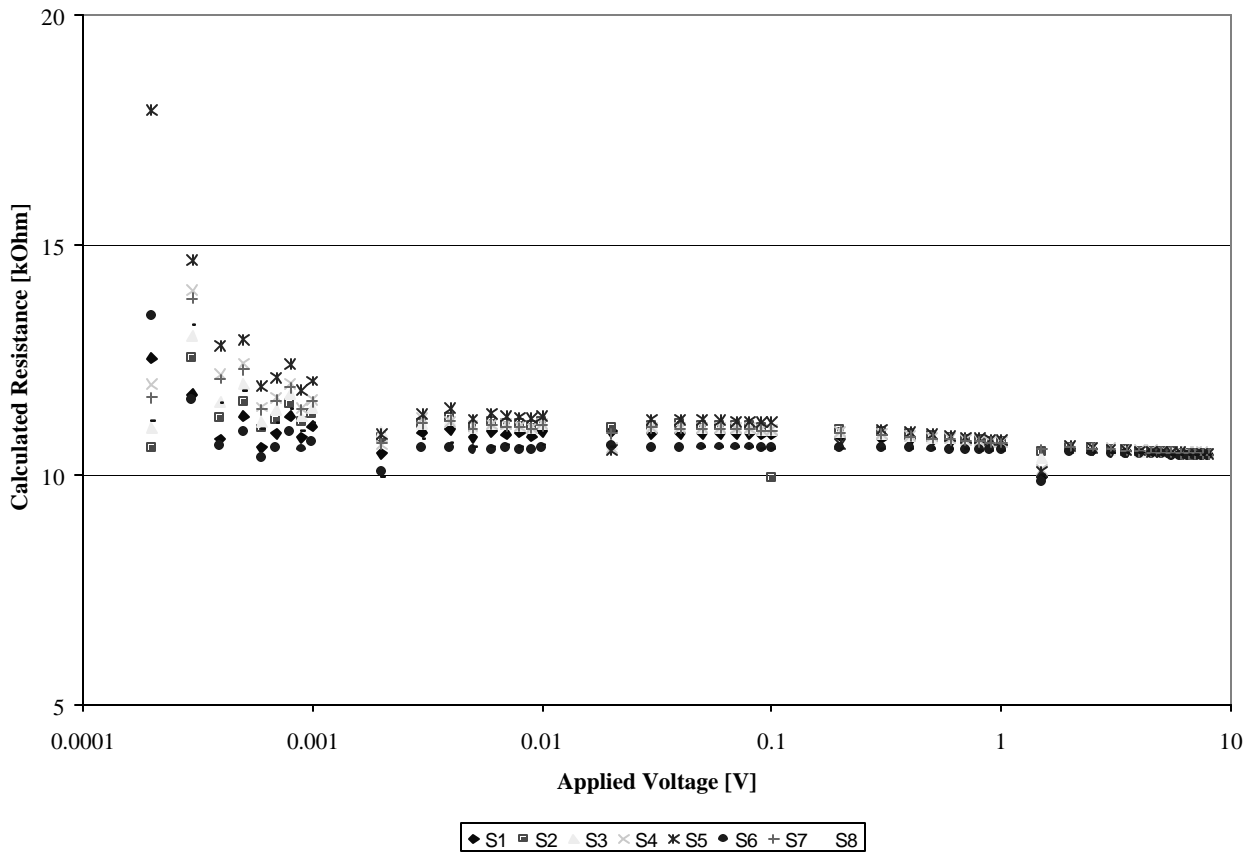
Figure 16: Standard resistor bench test (with switches)

Chip Preparation and Characterization

Chip preparation consisted of removing the transducer housing, extracting the

chip, slicing the manufactured chip mount, remounting the chip on standard dips, and

wire bonding gold wires from the dip posts to the chip contact pads. The removal and

extraction of the chips occurred in the laboratory at Air Force Institute of Technology

(AFIT). The slicing, remounting, and wire bonding took place at the Air Force Research

Laboratory (AFRL), also at the Wright-Patterson Air Force base.

A standard Dremel® tool was used to breach the transducer housing. Once the

transducer housing was sufficiently reduced, the piezoresistive chips were removed,

cleaned in alcohol, and taken to AFRL (see Figure 17). At AFRL, a diamond blade axial saw was used to slice the chip mounts to within approximately 1mm from the chip. Following the slicing stage, the chips were again cleaned in alcohol and remounted to standard dips with epoxy. Once the chips were remounted, a bonding machine was used to bond gold wires from the dip posts to the contact pads on the chip (see Figure 18).
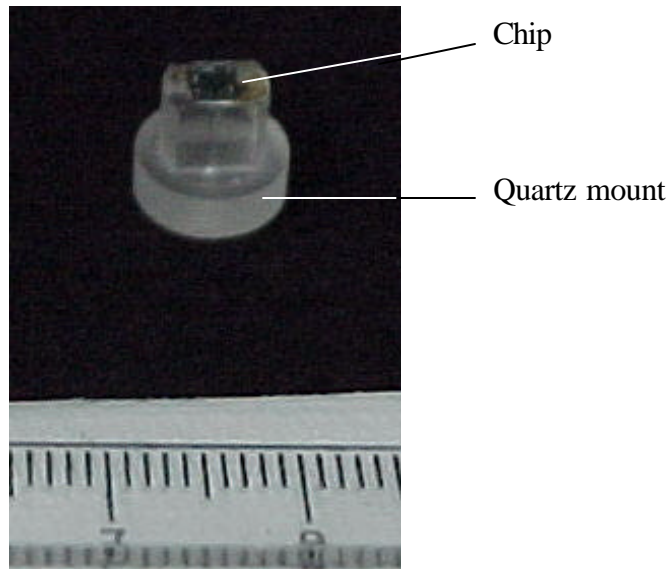
Figure 17: Piezoresistive chip
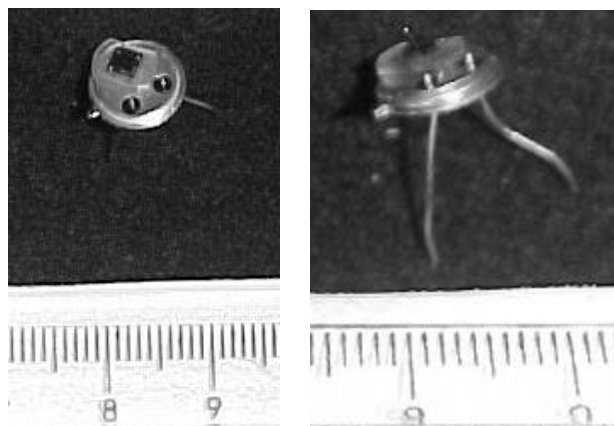
Figure 18: Piezoresistive chip on transistor mount (top and side view)

33

In a similar fashion as the measurement system characterization, the chips were characterized by running a sequence of voltage sweeps across each chip. This allowed for the determination of each chip's baseline response as a function of applied voltage.
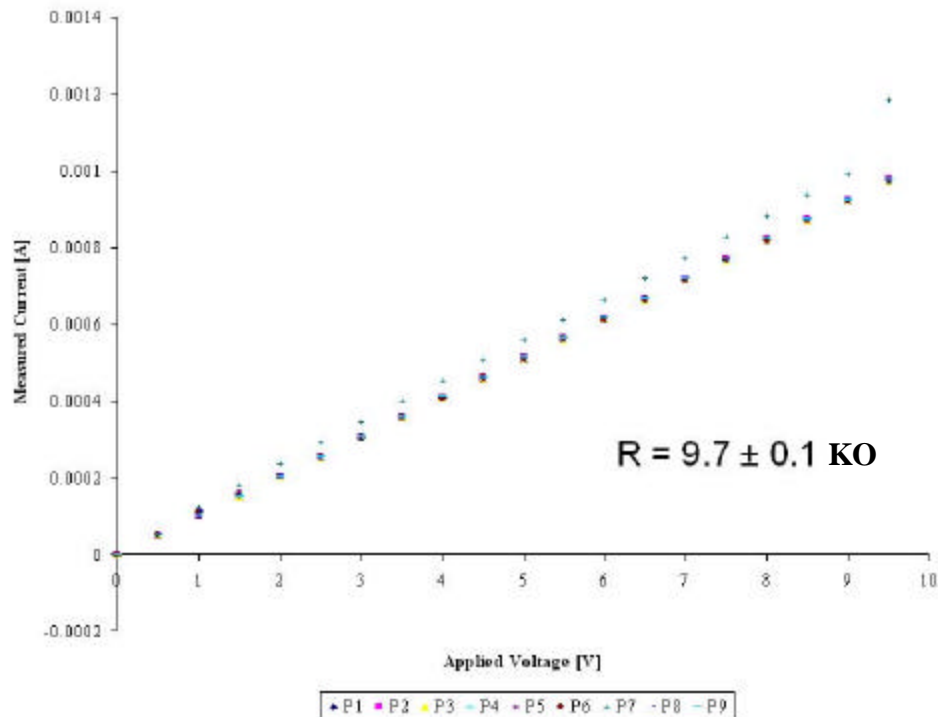
Figure 19: Baseline piezoresistive chip characterization

Irradiation Tests

This research considers two radiation environments: gamma ray only environment (provided by a standard gamma cell employing a ^{60}Co source), and a mixed, neutron and gamma ray environment (provided by a research reactor). The gamma ray only environment is included in the study because in-situ measurements in the reactor environment must account for the gamma dose received. Specifically, the Compton

34

current generated by the ionizing radiation as a function of dose must be subtracted from the in-situ current measurements taken from measurements taken during irradiation in a mixed field. Here, the neutron dose contribution to the Compton currents is considered to be negligible. The Compton current is expected to scale linearly with gamma dose under two conditions: the dose rate remains in the Low Level Injection (LLI) regime and saturation is not achieved.

In order to uncouple the Compton current from the current measurements taken during the reactor irradiation tests, four chips were irradiated in the gamma cell to a maximum total dose of $1Mrad_{Si}$. In order to characterize the annealing behavior of the chips as a function of total dose, one chip was removed from the radiation each time a $250Krad_{Si}$ interval was reached.

Both the gamma cell and the reactor irradiation tests took place at the OSURR facility. Appendix A contains extracts from the irradiation test plan and explains in greater detail the conduct of the irradiation tests. In essence, the irradiation times were computed for the irradiation cycles in the gamma cell and the reactor in order to achieve the target total dose. A target total dose of $1Mrad_{Si}$ was selected based on time for the gamma cell tests. This was done primarily because of the low dose rate present in the gamma cell compared to that of the beam port. The target neutron total dose of 4 MradSi was selected based on initial results from the Sandia ACRR tests.

Prior to the start of the piezoresistive chip tests, the neutron flux at beam port #1 was characterized using the foil activation technique. This was done in order to obtain an estimation of the dose rate at beam port #1 as a function of reactor power. Once the dose rate at beam port #1 was determined, the chip irradiation tests proceeded as planned.

Although the test plan calls for the reactor tests to occur sequentially, due to time constraints and concerns about the safe handling of the devices following cooling, the first reactor test consisted of only irradiating one chip to 1 Mrad$_{Si}$. This was done in order to gain a benchmark of the exposure levels prior to and following the cooling period owing to the activation of the test mount and chips. In order to get the remaining three chips caught up to their intended dose levels, the first irradiation cycle conducted on the following day included ran for twice as long. This resulted in achieving the intended 2 Mrad$_{Si}$ at the end of the irradiation cycle.

Annealing

As specified in the irradiation test plan, once a 25-percent interval of the total dose had been achieved, the test mount was removed from the radiation and one device was transferred to the annealing station. Upon removal from the radiation, annealing began instantaneously in all devices. Therefore, the test control program was not paused until one full measurement cycle was completed in order to capture device performance upon removal from the radiation. Once the device transfer was accomplished and connectivity checks verified that the CPU was receiving a response from the transferred device, the test control program was allowed to continue.

In the case of the reactor irradiation tests, at the end of an irradiation cycle, the reactor was powered down and all devices experienced a one-hour *cooling* period. This allowed for the safe handling of the irradiated chips and activated mounting materials. Once the reactor was powered down, the neutron flux is assumed to be negligible. Analysis, however, must account for the gamma radiation streaming off of the reactor core during this cooling period. Similarly, analysis must account for the gamma dose

received by the chips upon insertion into the beam port, prior to the start-up of the reactor. The gamma flux prior to reactor start up during these periods is considered to be constant.

During the irradiation cycles, the annealing chips are incorporated into the measurement cycle. Once all irradiation cycles were completed and the final chip was transferred to the annealing station, the test control program utilized an exponential function to gradually increase the length of time between measurements. This was done because of the exponential form of the annealing factors. The desire to characterize device performance during annealing requires more measurements at early times, and fewer measurements at later times.

Analysis Procedure

The analysis procedure begins with a FORTRAN program that first parses the data files. As shown in Appendix D, this creates a set of data files that are easily imported into computer software. During a second conditioning run through the FORTRAN program, the data file's time stamp was converted into a time that referenced the start of the initial irradiation cycle. In this fashion, the results from a particular data file coincide with the dose received at the time the measurements were obtained.

In order to arrive at the change in resistivity, the data files were imported into Mathcad (2001 Professional edition) and manipulated further. From Ohm's Law, the change in resistance at an applied voltage, V, is given by:

$$\Delta\rho = \frac{V}{I_m} - \frac{V}{I_o} \tag{21}$$

where I_m is the measured current, I_o is the initial current (from baseline measurements). The change in resistivity is obtained from equation (21) by further dividing by the initial resistivity. Resistivity expresses resistance in terms of length of material traversed and the cross sectional area normal to the path of the charge carriers. As shown in equation (22), however, the fractional change in resistivity as given in equation (21) also equates to the fractional change in resistance (as long as the path length, L, and area, A, remain constant).

$$\frac{\Delta\rho\left(\dfrac{L}{A}\right)}{\rho_o\left(\dfrac{L}{A}\right)} = \frac{\Delta R}{R_o} \tag{22}$$

Standard deviations were computed using the population standard deviation equation given by:

$$\sigma_{\Delta\rho} = \sqrt{\frac{1}{N}\sum_{i=1}^{N}\left(\Delta\rho_i - \Delta\rho_{mean}\right)^2} \tag{23}$$

where N is the total number of samples at a particular time (dose), $\Delta\rho_i$ is the change in resistance at the specified time of sample i, and $\Delta\rho_{mean}$ is the mean change in resistance at the specified time. In order to compute the standard deviation of the mean, $s_{\Delta\rho}$ is further divided by the square root of the number of samples.[23] Although equation (24) is written in terms of the change in resistance, the same form of the equation was used in the

estimations of the uncertainty in the current measurements. The uncertainty in the dose

rate calculations is obtained by applying the following general rule in error propagation:

$$\sigma_a = \sqrt{\left(\frac{d}{dx}a\right)\sigma_x^2 + \left(\frac{d}{dy}a\right)^2\sigma_y^2} \tag{24}$$

where a is the known multi-term function of independent variables (here x and y), the

derivative terms are in fact the partial derivatives of the given function, and the s^2 terms

are the squares of the uncertainty in the independent variables.

IV.   Results

The results obtained during this research consist of the verification of the initial model, results obtained from the gamma cell and beam port irradiation tests, and the identification of points at which the model fails.

Initial PISCES-II Model

Running the PISCES-II code with the physical parameters of the model and 10^{19} cm^{-3} as an initial guess for dopant concentration resulted in a refinement of the dopant concentration. In comparing the estimated current from the PISCES-II output to the baseline current at 8V, a dopant concentration of 4.75 10^{18} cm^{-3} is required in order for the expected current to agree with the measured current.

Gamma-only Irradiation

Table 2 shows the total dose received by each of the chips. While P5 received a total dose of 500 Krad$_{Si}$, the chip fell off of the test mount's 124-pin dip mount. As a result, the in-situ measurements could not be obtained from P5 during the second irradiation cycle. As the CPU could no longer gain connectivity with P5 after the second irradiation cycle, it was assumed that at least one of the wire bonds connecting the chip to the dip broke when the device fell to the bottom of the test mount (this was later confirmed using a standard ohm-meter).

Table 2: Gamma Cell Total Dose Distribution

Chip	Total Dose (Mrad$_{Si}$)
P1	1.00
P2	0.25
P5	0.50
P4	0.75

Figure 20 shows the raw data obtained from device P1 during the first irradiation cycle. As seen in the figure, the measured current does not appear to vary as the total gamma dose received increases. When the values of the measured current are compared to the base line current measurements in Figure 19, however, it is evident that the changes occur in the μA range (see Figure 21).
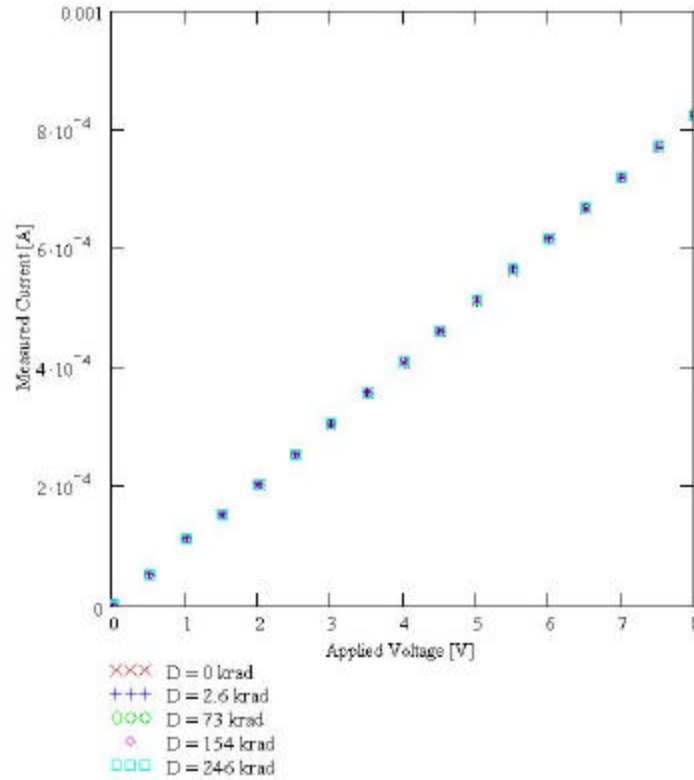
Figure 20: P1 response during first irradiation cycle
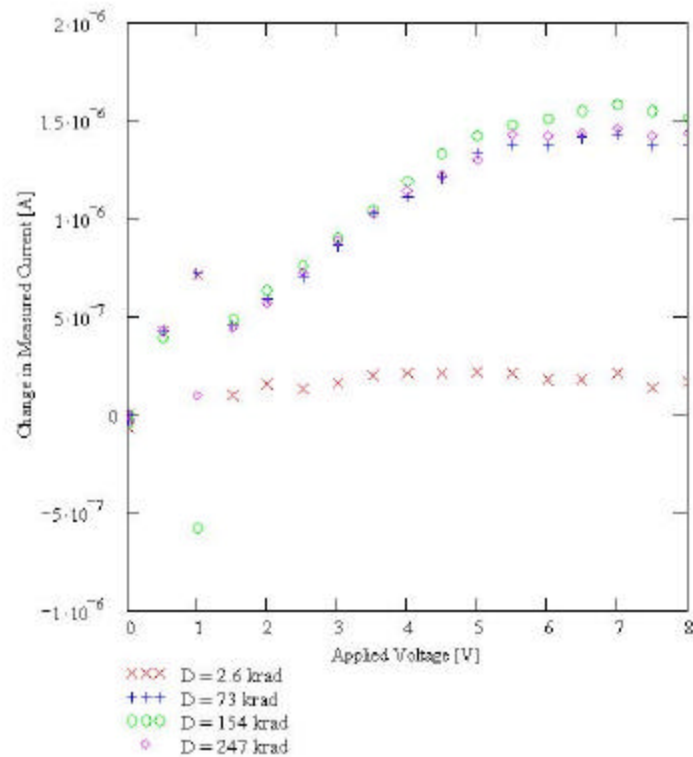
Figure 21: Change in measured current

Figure 22 shows the calculated results from the gamma cell irradiation obtained by using equations (21) and (22). As indicated in the figure, the first 97 minutes comprise the first irradiation cycle. At the end of the first cycle, the test mount was removed from the radiation and device P2 was transferred to the annealing station. Data from device P4 was disregarded as the initial results indicated extreme non-linear response at all applied voltages during the three irradiation cycles for which it was irradiated. It is entirely possible handling of the device pressed the wire bonds against the silicon based to which the chip is mounted. This created a secondary electron path between the dip pins that contributed to the current measurements and masked the desired current measurement.
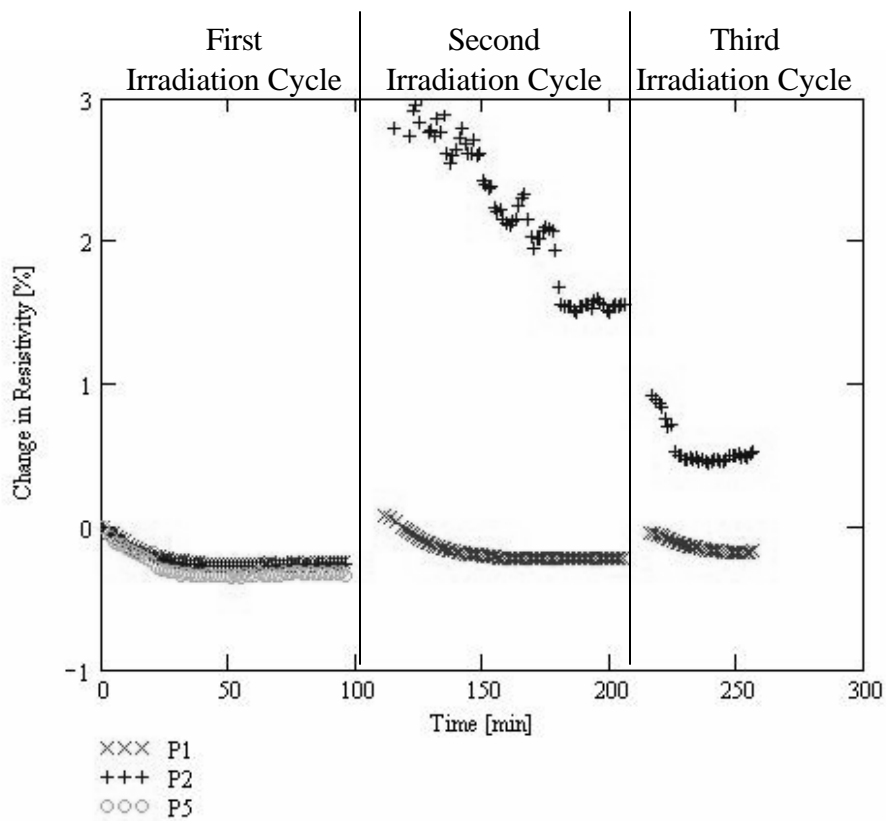
Figure 22: Gamma Cell Irradiation Results

As indicated in Figure 22, device P2 exhibited a large positive overshoot during its annealing which decayed with time. However, only the first irradiation cycle provides statistically reliable information. The two devices remaining after the first cycle offer only one sample data set (P2 for annealing and P1 during irradiation). After 256 minutes, the voltage sweep parameters were erroneously set below the error threshold. Had the voltage sweep parameters not been altered, the annealing profile of P1 could have been compared to that of device P2.

As developed previously, the Compton current scales linearly with dose rate, provided electron-hole pairs generated falls in the LLI regime. For the p-type silicon used in the Ametek piezoresistive chips, the LLI regime ends at approximately 11Krad$_{Si}$.

43

As a result, the measured current is expected to follow a non-linear relationship as a function of dose above this level.[10]

While the estimated current from the PISCES-II code agrees with the baseline current measurements, the active volume of the entire chip is required in order to account for the photocurrent during gamma irradiation.

Neutron and Gamma Irradiation

Unlike the gamma cell irradiation tests where essentially two devices were destroyed, during the neutron irradiation tests only device P10 displayed extremely non-linear behavior as a function of applied voltage and total dose received. P10 was also the device that was irradiated separately. Table 3 shows the level to which the chips were irradiated during the reactor irradiation tests. The error in the total neutron dose received is estimated to be 0.06 $Mrad_{Si}$.

Table 3: Neutron total dose distribution

Chip	Total Dose ($Mrad_{Si}$)
P6	3.00
P8	4.00
P9	2.00
P10	1.00

Figure 23 shows the measurements obtained during the beam port irradiation cycles. The figure also indicates the reactor power cycle. As expected from neutron induced displacement damage, the measured current decreases while the reactor is at power.
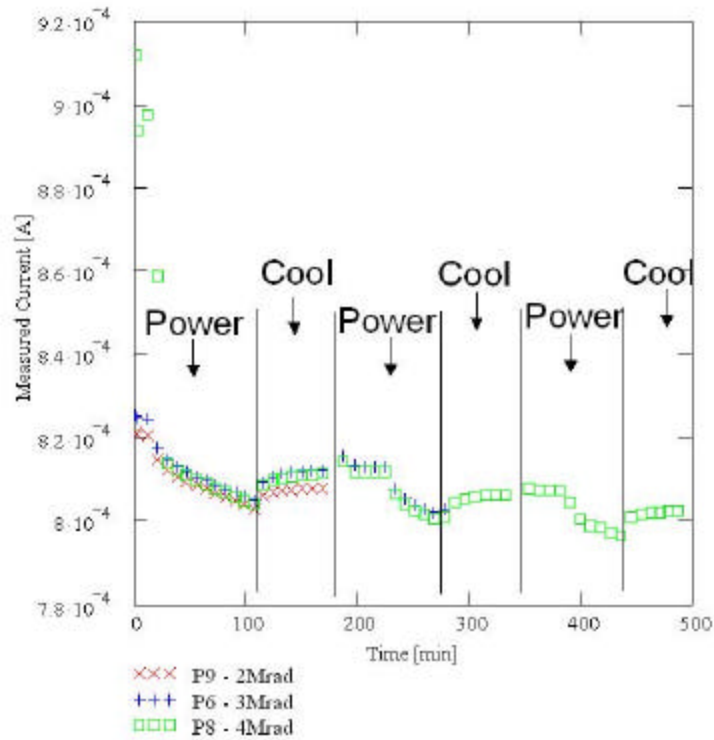
Figure 23: Beam port measurements

Generated by using Equations (20) and (21), Figure 24 shows the mean change in resistance as a function of time (dose). Because the electron-hole pair generation rate in the beam port (where the gamma dose rate is approximately 1800 $Krad_{Si}$ hr^{-1}) is in the HLI regime, the active volume is no longer restricted to the p-channels and the results are displayed in terms of the resistance. The associated uncertainties are not plotted with the data points as they generally ranged between 0.0004% and 0.003%. The associated uncertainties in the in-situ data points obtained during the third irradiation cycle (from three to four $Mrad_{Si}$) are unknown, however, it is estimated to be on the order of 0.003%.
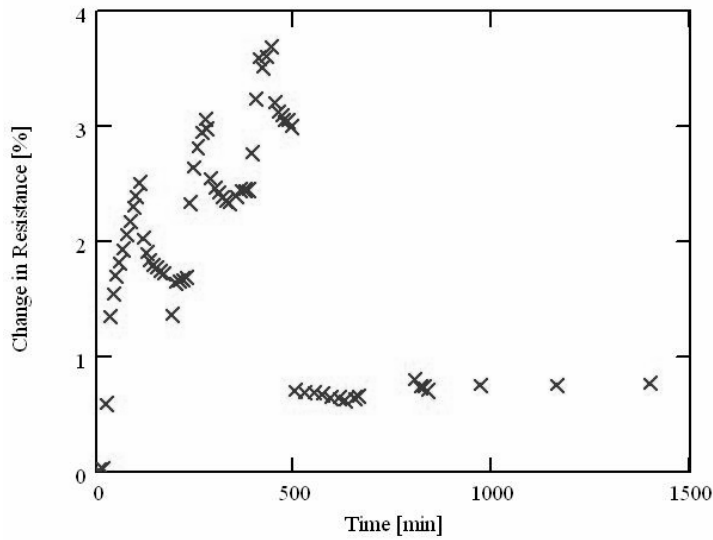
Figure 24: Reactor irradiation results

Figure 24 displays only the mean change in resistance as a function of time (dose). Clearly evident in the figure are the exponential rise in resistance due to displacement damage and the exponential decline in resistance as displacement defects anneal. The periods of exponential annealing coincide with the cooling periods during which the chips remained in the beam port.

In order for the change in resistance to remain positive during the cooling period, the characteristic time for the annealing of the displacement damage must be on the order of tens of minutes. Otherwise, the gamma flux in the beam port would cause a purely negative change in resistance as seen in the gamma cell tests. No gamma dosimetry measurements were performed on the beam port during the cooling period.

The change in resistance does not decline to permanent levels until the chips were removed from the radiation environment. This implies that the excess charge carriers

46

produced by the ionizing radiation occupied the dominant defect sites. Once the excess

charge carriers recombined, further annealing was possible.

Figure 25 shows the change in resistance during irradiation as a function of dose.

Also depicted is the permanent change in resistance observed following isothermal

annealing.
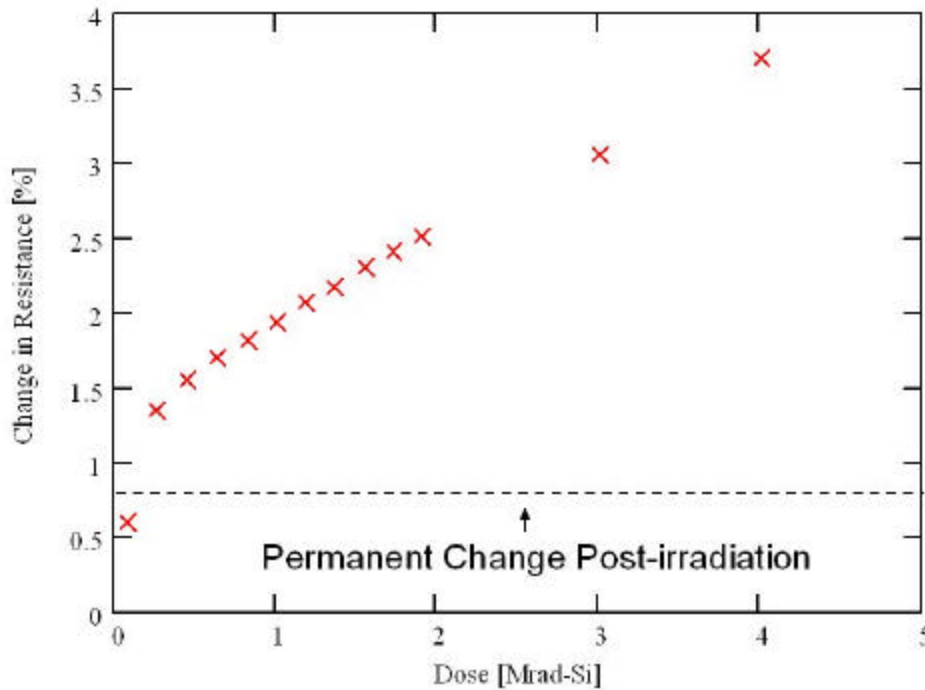
Figure 25: Change in resistance as a function of neutron dose

The temperature in the beam port did not rise more than 15 $^{\circ}$C above room

temperature during the course of the irradiation cycles (as shown in Figure 26). This

change in temperature equals a change in energy of only 0.001eV. Therefore, chip

heating during irradiation can be neglected.
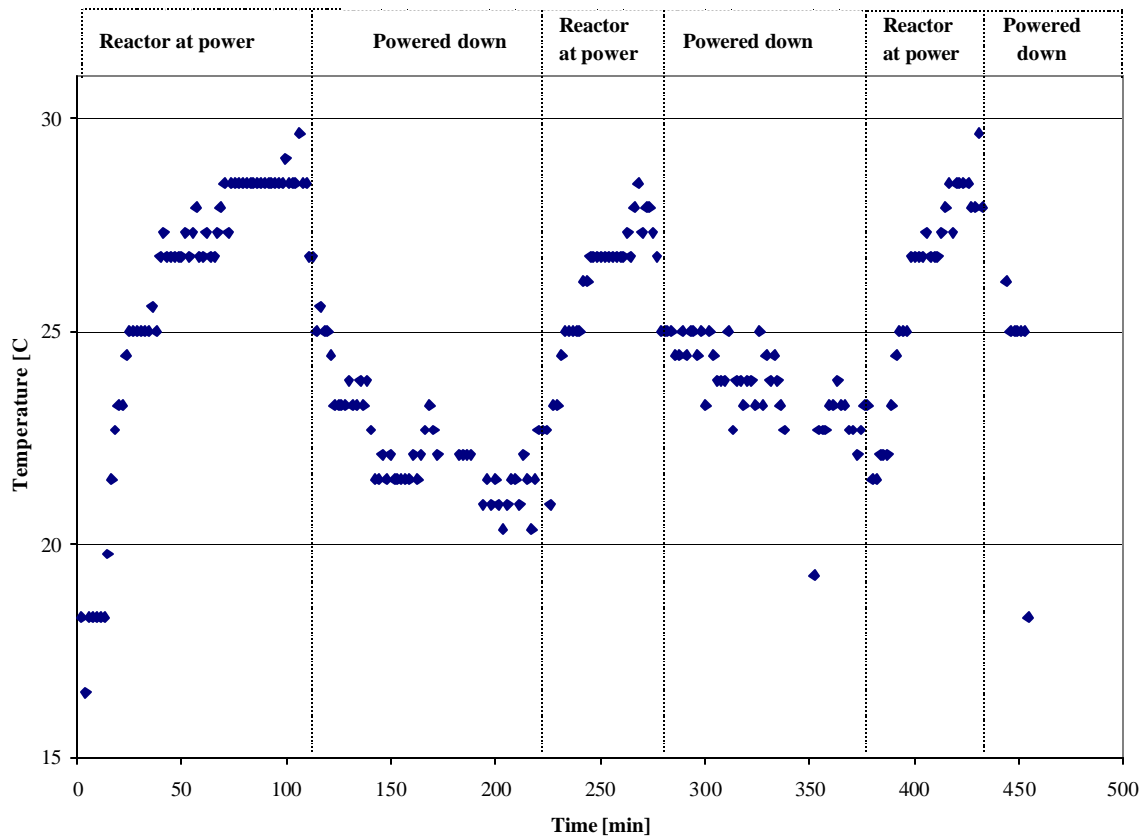
Figure 26: Temperature profile of beam port #1

Identification of Transducer Vulnerabilities

Based on this research, several key aspects of the effects of ionizing and non-ionizing radiation on piezoresistive pressure transducers warrant discussion. As demonstrated by the gamma cell irradiation tests, the magnitude of the Compton current generated by ionizing radiation extends into the microampere range. While common transducer signal conditioning devices (i.e.: voltage regulators and differential amplifiers) pass currents in the milliampere range, the potential exists for excess currents to exceed design parameters. In addition, once the HLI regime is reached, the active volume can extend to the entire chip.

48

The inclusion of signal conditioning devices within the transducer itself presents further opportunities for device failure. Metal-oxide-semiconductor (MOS) devices in particular can experience extreme changes in their operating parameters as a result of the radiation dose they receive. Transistors predominantly experience a shift in their threshold voltage, whereas MOS capacitors experience a shift in the flat band voltage. Leakage currents also increase in MOS devices as a function of ionizing radiation dose.

Initial concerns from Ametek regarding the stability of the silicon mount (in which the chip is embedded) in a gamma ray environment were not observed. While the color of the silicon mount changed from clear to brown as a result of neutron interactions, no physical effects of gamma radiation were observed.

Extension of Results to ACRR Shots

Appendix C contains detailed information regarding the tests conducted at the Sandia ACRR by the researchers at LANL. In order to arrive at an estimated dose rate, the pulse yield (in MJ) profile was integrated with respect to the pulse width in order to obtain an average yield rate. A neutron fluence normalization constant was used in order to estimate the total neutron flux. An estimated differential flux was obtained by using the estimated total flux multiplied by the relative neutron distribution (normalized to 1 neutron cm^{-2} s^{-1}) provided by Sandia and dividing by the average group energy.[24]

The estimated neutron dose rate for the May 2001 tests at the ACRR is 170 ± 10 $Mrad_{Si}$ hr^{-1}. With a pulse width of 123.2ms, this results in a total neutron dose of 5.9 ± 0.4 $Krad_{Si}$. Similarly, using a gamma dose normalization constant, the estimated gamma dose delivered by the pulse is 260 ± 60 $Krad_{Si}$.

In comparing the dose delivered by the pulses generated in the ACRR to the dose delivered in the reactor at OSU, the ACRR total neutron dose of approximately 6 $Krad_{Si}$ would be achieved at the OSU reactor in 14 seconds. From the results depicted in Figure 24, the change in resistance reached the permanent damage threshold between 11 and 20 minutes following the start of the irradiation. This corresponds to a dose between 232 and 422 $Krad_{Si}$.

The estimated gamma dose delivered by the ACRR pulse corresponds well with the first irradiation cycle performed in the gamma cell. This implies that a correction factor can be applied to the transducer output in order to account for the Compton current generated by ionizing radiation (as long as the current was limited to the p-channel). A somewhat lower saturation level is expected from a pulse of ionizing radiation in the ACRR than the one shown in Figure 22. This is because the gamma flux is much larger at the ACRR than at the OSU reactor. A greater density of electron-hole pairs are generated in a shorter amount of time implies more recombination occurs.

Other Observations

In examining the effects of non-ionizing radiation on the resistance of the piezoresistive chips, it becomes clear that even with a dose of 4 $Mrad_{Si}$ the p-channel is capable of passing current. With only a 3.7% change in resistance during irradiation and a permanent change in resistance of 0.8%, there are two plausible explanations for cause of chip failure.

First, this research did not examine the chip's piezoresistive response as a function of total dose. It is entirely possible that even with correction factors applied to the output signal as indicated above, the displacement damage from non-ionizing

50

radiation and the current generated from ionizing radiation alter the crystal's ability to respond to pressure. From Smith's hypothesis regarding the nature of the piezoresistive effect and electron-phonon interactions, it follows that any process that alters the interactions will also alter the piezoresistive response of a crystal.

Second, the source of transducer failure as a result of irradiation lies outside of the chip. As shown with Ametek's transducer design, many additional components may be added to the transducer circuit aside from the piezoresistive chip. While the specification sheets for the transducers used by LANL do not indicate the presence of any signal conditioning devices, some do contain temperature compensating resistors.[25,26]

V. Research Summary

In summary, this research consisted of the design and characterization of the measurement system, the preparation and characterization of the test chips, and the planning and execution of the irradiation test plan. The irradiation tests were conducted at the Ohio State University research reactor facility.

The principle outcome of this research is that the primary mode of transducer failure in radiation environments is not a change in the bulk resistivity of the piezoresistive chip. At the maximum neutron total dose of 4 $Mrad_{Si}$, the peak change in resistance was approximately 3.7%. This research suggests that at dose levels above 1 MradSi, a permanent change in resistivity of 0.7% is observed (at room temperature).

Conclusions

Ionizing Radiation Damage

The ionizing radiation tests performed in the gamma cell allowed for the characterization of the magnitude and time scale of Compton current generation in p-type silicon (0.016 O-cm). The temporary change in resistivity is directly attributable to Compton current generation. Also observed was the effect of HLI in which the active volume extended beyond the p-channel and included the entire chip volume. Statistically significant insights into the effect of ionizing radiation at total dose levels above 250 $Krad_{Si}$ and into the annealing behavior could not be achieved due to the physical failure of two chips during testing.

Displacement Damage

The mixed radiation environment tests allowed for the measurement of the change in resistance as a function of total neutron dose. The expected increase in resistance due to displacement damage was observed during irradiation. While the displacement damage appeared to anneal exponentially while the chips were cooling prior to handling, the change in resistance dropped nearly to the permanent level of 0.7% immediately upon removal from the beam port. This implies that the excess charge carriers must occupy the dominant defect sites and prevent further annealing until all the excess charge carriers have recombined.

Applications

The insights gained during the course of this research apply directly to the application of piezoresistive pressure transducers by LANL. The demonstrated impacts of ionizing and non-ionizing radiation extend to any application of piezoresistive transducers operated in a radiation environment.

While the use of correction factors may be possible, the correction factors must be developed while taking the specific type of chip and the nature of the radiation environment into account. In cases where the intended current is not restricted to the p-channel during HLI, device output should be regarded as suspect. Furthermore, all signal-conditioning devices must be removed from the transducer and placed external to the radiation.

Recommendations for Future Research

Several key areas of this research warrant further investigation. This research clearly identifies the need to characterize the piezoresistive response and to gain more insight into the time scale at which annealing occurs in piezoresistive chips. In order to determine whether or not radiation damage within the chip causes transducer failure, the piezoresistive response must be characterized as a function of total dose.

This research was conducted using isothermal conditions. A study of the piezoresistive response as a function of total dose might also include an investigation of the impact of temperature on the recovery of the piezoresistive response.

The time interval between successive measurements on the same chip was on the time scale of minutes (1.5min on average). Because the measurement system could not cycle through the devices quickly enough, all of the data points are greater than one minute apart. A faster measurement cycle with fewer devices to sample would produce data points with a time spread on the order of milliseconds or less.

Appendix A. Extracts from the Irradiation Test Plan

Test Objectives

The planned tests investigate the piezoresistive response of silicon to doses of

ionizing and non-ionizing radiation delivered by the OSURR and a gamma cell

(collocated with the OSURR). The tests are designed to characterize the performance of

a piezoresistive chip in a radiation environment as well as its behavior while annealing at

room temperature. The objectives of this experiment are (in order of precedence):

1. Determine baseline resistivity change as a function of total dose
2. Characterize annealing behavior as a function of time at room temperature
3. Characterize the change in piezoresistive response as a function of total dose
4. Characterize the change in piezoresistive response during annealing at room temperature
5. Determine the level of dopant activation (if any) as a result of neutron capture and identify the dopant.

This experiment uses Ametek piezoresistive transducer chips produced by the

same manufacturer and of the same transducer model. A brief discussion of the tests to

be conducted and the expected results follows.

Basic Device Physics Tests

The piezoresistive transducer chips tested in this experiment are designed similar

to that as depicted in Figure 27. The silicon measures approximately 0.28mm square and

is approximately 50μm thick.
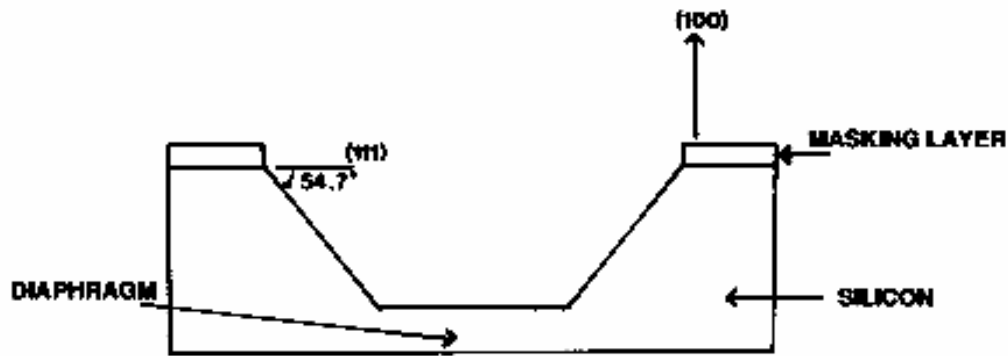
Figure 27: Piezoresistive transducer construct (side view)

For stability, the silicon chip is mounted to a quartz crystal, which is not connected to the transducer's main circuit board (see Figure 28). The main circuit board consists of a capacitor, a voltage regulator, a quad-operating amplifier, two diodes, and a series of temperature compensating, thin-film resistors.
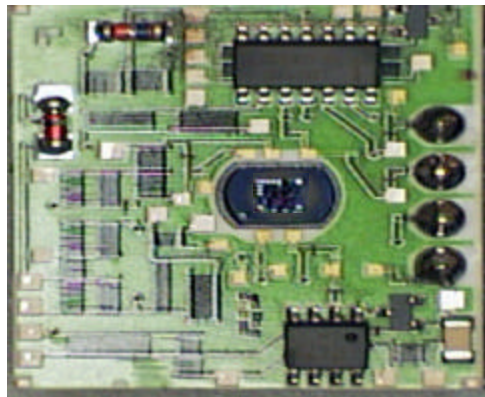
Figure 28: Piezoresistive Transducer Circuit Board

In an effort to determine the effects of ionizing and non-ionizing radiation on the performance of a piezoresistive chip commonly used in transducers, the chips from manufactured transducers will be removed from their circuit boards. The chips will be mounted on to a test platform designed specifically for this research. The piezoresistive transducer chips selected for this experiment are representative of a commonly accepted

design for converting an applied pressure into an electronic signal. This particular model

is designed to accept 12-25V input and transmit an output signal in the range of 1-5V. In

this experiment, however, all of the transducer's onboard signal conditioning and voltage

regulating electronics will have been removed. The piezoresistive chip consists of a base

of n-type silicon with a p-type silicon circuit (Wheatstone bridge) embedded in one side

(see Figure 29).

The embedded contact points are evident in Figure 29. At this time, the contacts

are most likely made of Indium, however, there may also be trace amounts of gold

embedded in the chip as well. It is also currently unclear whether the silicon chip is

doped with Boron or Phosphorus (or some other element). The dopant concentrations are

also unknown at this time.

Figure 29: Enlarged Ametek piezoresistive Chip (top view)

I plan to investigate the two primary dose effects on the piezoresistive chip. First,

I will investigate the Compton current generated as a function to total dose in the gamma

cell. Second, I will investigate the displacement damage as a function of the non-ionizing

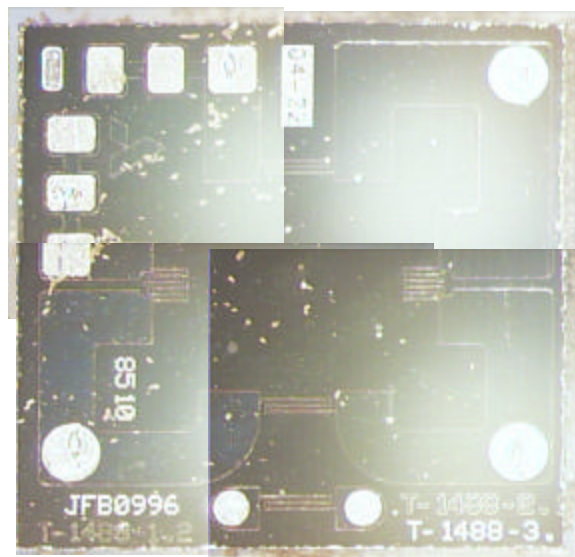radiation total dose.

Description of Tests

This experiment consists of six principle tests. Test A1 consists of performing in-situ measurements while the devices are in a gamma-only radiation. In test A2, measurements are taken while the A1 test devices are annealing at room temperature. Test B1 consists of performing in-situ measurements while the devices are irradiated near the reactor core (neutron and gamma radiation). Test B2 consists of taking measurements while the B1 test devices are annealing at room temperature. Test C1 is a dosimetry test used to characterize the neutron flux present during the B1 test and runs concurrent with the B1 test.

All of the in-situ tests in this experiment rely on simple I-V measurements. A Keithly 237 signal measurement unit (SMU) will source a voltage (applied to the piezoresistive chip) and measure a current. A laptop computer will be used to control the SMU and store data. The program will also control a series of electric switches (external to the radiation) designed to select devices being measured by the SMU. When the temperature measurements are desired, the laptop maintains device #8 as the thermocouple device and executes a temperature measurement at the beginning of each measurement sweep. Appendix A contains a flow chart depicting the program sequence.

Pre-Irradiation Shakedown and Debug Tests

Prior to irradiation, all devices will be characterized in the laboratory at AFIT. All transducer chips will be tested in the test configuration to determine any initial

variability. This will also help in the shakedown of any software bugs. The baseline measurements allow for the determination of the initial resistivity of the piezoresistive chip and the change in resistivity with an applied pressure.

Test A1: Gamma-only Irradiation (Gamma Cell) Test

In test A1, the devices will be lowered into the gamma cell to a height of 8 inches from the bottom and irradiated for a total of 6 hours and 32 minutes (until a maximum total dose of 1.0 Mrad$_{Si}$ has been delivered). As each 25% interval of the total dose is reached, the devices will be raised and one will be moved to the annealing station. Once the device has been inserted into the annealing station and the control program configured to reflect the move, the remaining devices will be lowered back into the gamma cell and the program will continue until the next 25% interval is reached.

Test Configuration

Figure 31 in Annex A-2 shows the test configuration for test A1. The laptop is connected to the control box via the LPT port, and to the Keithly SMU via the GPIB interface card. Coax cables from the hobby box to the control box provide connectivity between the SMU and the test devices. The test devices are mounted to a hobby box via dip connectors inserted into an external breadboard. Thermocouple wire connected to a coax cable allows the SMU to measure the temperature at the devices during irradiation. Optoisolators within the control box, powered by the status of the LPT output pins, control which test device is connected to the SMU.

Test Procedure

Test A1 consists of the following steps:

1. Power SMU and HP
2. Run piezoresistive Test Initialization program
3. Configure SMU and HP
4. Connect devices to hobby box
5. Connect coax cables to hobby box and control box
6. Connect resistors at device locations of annealing station
7. Run connectivity routine and ensure program registers eight devices and the SMU
8. Remove the resistors from the annealing station
9. Start piezoresistive Test Control program
10. Configure sweep information and output file location
11. Select devices being irradiated
12. Lower hobby box into gamma cell
13. Start measurement
14. When 25% interval of max dose is received, pause program
15. Raise hobby box and move one (1) device to annealing station
16. Re-configure piezoresistive Test Control to reflect the move
17. Repeat step 12 until all devices have been moved.
18. Allow program to run until ready for test B1

Possible Problems/Complications

The (γ,n) cross section in the radiated materials (primarily plastic, metals, and silicon) is extremely low at the gamma energies expected (with a maximum of 1.33MeV from the beta-decay of the ^{60}Co). As a result, photonuclear activation is not expected to be an issue in this test.

Of primary concern are the loss of a device in the gamma cell and a computer "lock up". The device mount is designed to firmly grip each device. Prior to lowering the hobby box into the gamma cell, each device will be checked to ensure that it is properly seated and cannot be knocked out of the mount. The program will be periodically checked throughout the test to ensure that it is functioning as designed.

Test B1: Neutron and Gamma Irradiation (reactor) Test

In test B1, the devices will be inserted into the reactor beam port and irradiated for four 47 minute periods until a maximum total dose of 4.0 $Mrad_{Si}$ has been delivered). As each 25% interval of the total dose is reached, the reactor will be powered down and the devices will be allowed to cool for 1 hour. Following the cooling period, one device will be moved to the annealing station. Once the device has been inserted into the annealing station and the control program configured to reflect the move, the remaining devices will be returned back into the reactor, the reactor will be brought back to power and the program will continue until the next 25% interval is reached.

Test Configuration

Figure 31 in Annex A-2 shows the test configuration for test B1. The test configuration for this test is the same as that used in test A1.

Test Procedure

Test B1 consists of the following steps:

1. Power reactor to 22.2 % (100 MW_{th})
2. Power SMU
3. Run piezoresistive Test Initialization program and start warm-up procedure
4. Configure SMU
5. Connect devices to test mount and attach paraffin plug
6. Connect coax cables to test mount and control box
7. Connect resistors at device locations of annealing station
8. Run connectivity routine and ensure program registers eight devices and the SMU
9. Remove the resistors from the annealing station
10. Start piezoresistive Test Control program

11. Configure sweep information and output file location (must use different file directory than that used in test A1 to prevent overwriting data!)
12. Select devices being irradiated
13. Insert test mount into beam port
14. Start measurement
15. When 25% interval of max dose is received, power down the reactor
16. Once the cooling off period has passed, deselect the device being removed from the test mount
17. Remove test mount from beam port and move one (1) device to annealing station
18. Return the test mount to the beam port
19. Re-configure piezoresistive Test Control to reflect the move
20. Power up the reactor
21. Repeat step 11 until all devices have been moved.
22. Pause program and select all eight (8) devices for annealing
23. Un-pause program and let run until annealing study is complete

Possible Problems/Complications

The primary concern with neutron irradiation is neutron activation. As a result, the experimental design is structured to limit the amount of activation products that might prevent handling of piezoresistive chips. Specifically, all unnecessary pins and wires will be removed from prefabricated components. The main elements present that are expected to activate are chlorine (in the plastic), gold, indium, and copper (in the wires and contacts).

Tests A2 & B2: Annealing Tests

The annealing tests will use the same program as the in-situ measurements. The computer will continue to run I-V measurements on the devices as they anneal and store the data. Test A2 will be temporarily halted during the B1 test. No action is required until the tests are completed.

Test C1: Dosimetry

Test C1 will be conducted concurrently with the B1 test in order to provide for dosimetry analysis. A gold wire will be mounted onto the B1 test mount during each irradiation period. At the conclusion of the B1 test, the gold wire will be analyzed using the OSU gamma-ray spectroscopy analysis system in order to calculate the flux required to produce the level of activation observed at the time of removal. Activation "start and stop" times will be noted when the test mount is removed from the reactor during B1 testing.

Special Requirements

Test Equipment

The planned tests require the following test and support equipment:

Test fixture box (2)
3" PVC pipe (5" diameter)
Electronic "hobby box" (1"x 2"x 1 ½")
Std breadboard (3) (Sized to fit test fixture boxes and hobby box)
¼" Plexiglas sheet
Keithly 237 SMU
Thermocouple wire (Type-K)
Coax cabling (8x20', 8x40')
10' 26-wire ribbon strip
Parallel port connector
Std multi-socket power strip
40' extension cord
Laptop w/GPIB card and MS Visual Basic
SMU interface cables (2) (one SMU-PC cable, one SMU-SMU series cable)
4N37 Optoisolator (8)
Pressure Transducer (10)
Gold wire

Gamma-ray spectroscopy system
Multi-pin dips and socket
Philips head screwdriver
Wire stripper
Soldiering Kit
Individual TLD
Radiation survey meter
Duct tape

OSU Gamma Irradiation Cell Conditions for Tests

Test A1 required that the gamma cell operate with all 14 ^{60}Co pins in place, providing a dose rate of approximately 153.3 Krad$_{Si}$/hr and an operational elevator (see Annex A-3 for gamma cell preliminary calculations). The gamma cell test mount will be lowered into the gamma cell to a height eight (8) inches above the bottom.

OSURR Conditions for Tests

Tests B1 and C1 require that the RR operate at 11.1 % power (50 MW$_{th}$) (see Annex A-3 for neutron dosimetry calculations).

Annex A-1.   piezoresistive Test Control Program Flow Chart

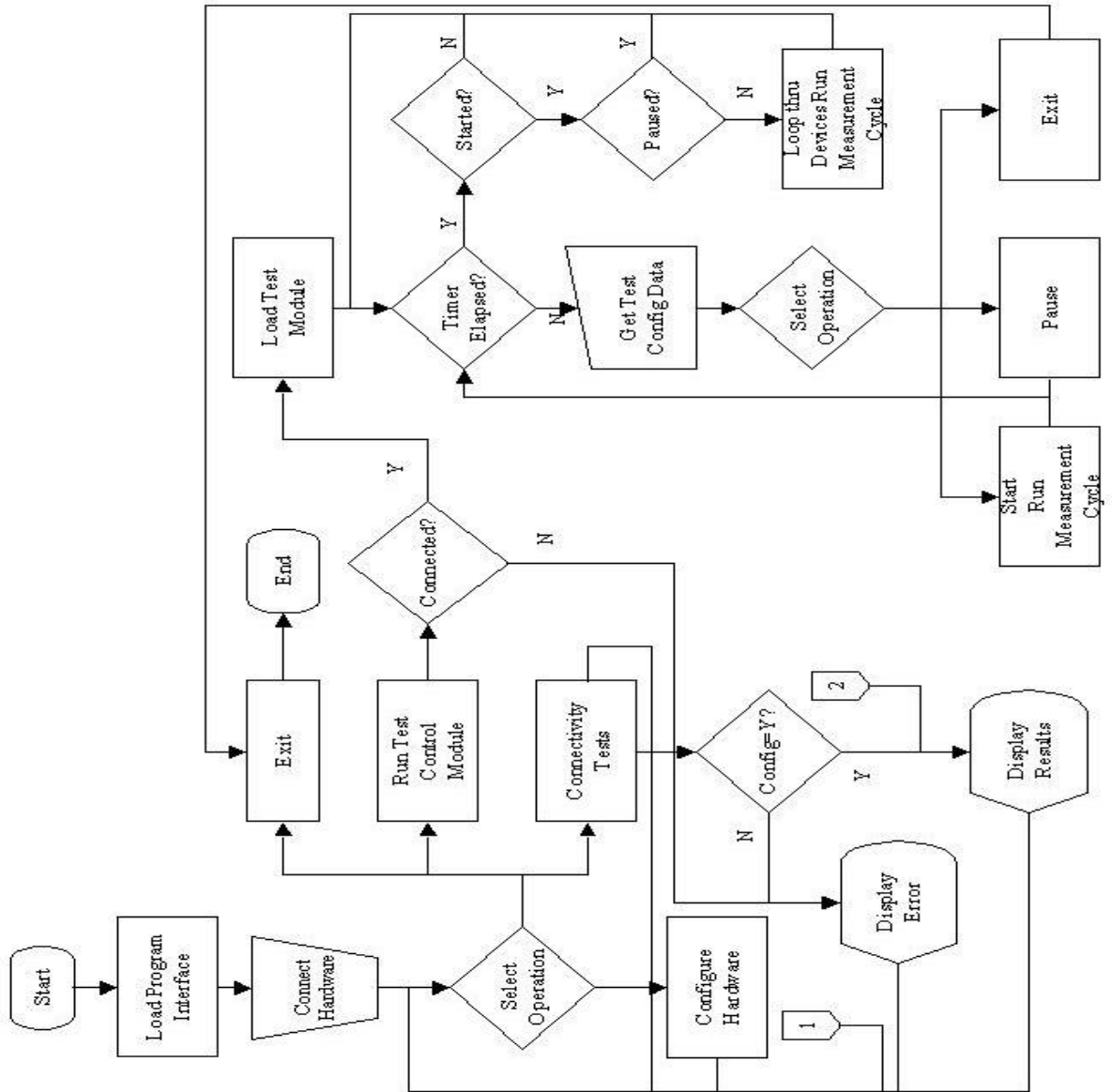Figure 30: piezoresistive Test Program Control Flow Chart
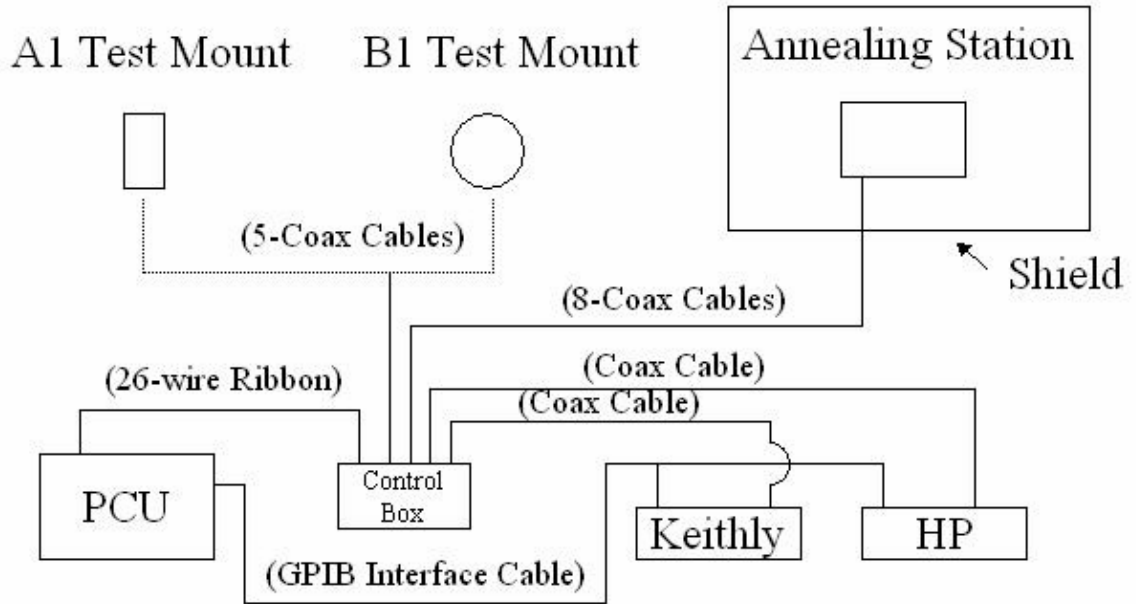
Annex A-2.   Test Configuration

Figure 31: Test Configuration

Annex A-3.   Preliminary Dosimetry Calculations

Gamma Cell Preliminary Calculations.

The gamma cell was calibrated on 28 January, 2002. The maximum dose rate

was calculated at a rate of 1.98kGy hr^{-1} using ceric-cerous dosimeters. First, the dose rate

is adjusted for the decay since the calibration date:

$$\Delta t := 318 \cdot day \qquad t_{half\_life} := 5.271 \cdot yr \qquad D_o := 1.98 \cdot \frac{kGy}{hr}$$

$$D_{rate\_\gamma\_H2O}(\Delta t) := D_o \cdot e^{\frac{-\ln(2) \cdot \Delta t}{t_{half\_life}}}$$

$$D_{rate\_\gamma\_H2O}(\Delta t) = 176.58 \frac{krad}{hr}$$

Next, the dose rate is calculated for silicon based on the ceric-cerous dose rate and

the ratio of the mass energy-absorption coefficients (MEAC) at 1.252 MeV:

$$\frac{D_{rate\_water}}{D_{rate\_Si}} = \frac{\left(\frac{\mu_{en}}{\rho}\right)_{water}}{\left(\frac{\mu_{en}}{\rho}\right)_{Si}} \qquad MEAC_{H2O} := 0.029639 \cdot \frac{cm^2}{gm}$$

$$MEAC_{Si} := 0.026511 \cdot \frac{cm^2}{gm}$$

$$D_{rate\_\gamma\_Si} := D_{rate\_\gamma\_H2O}(\Delta t) \cdot \frac{MEAC_{Si}}{MEAC_{H2O}}$$

$$D_{rate\_\gamma\_Si} = 157.944 \frac{krad}{hr}$$

The dose calculated above is multiplied by the attenuation factor for 1mm aluminum and results in a calculated dose rate of 156.89 Krad$_{Si}$ hr^{-1}.

Given the dose rate in silicon, the time need to achieve 1Mrad$_{Si}$ is calculated:

$$D_1 := 1 \cdot Mrad_{Si}$$

$$t_1 := \frac{D_1}{D_{rate\_\gamma\_Si}}$$

$$t_1 = 6.331\,hr \qquad\qquad t_1 - 6hr = 19.881\,min$$

The total time need to achieve 1 Mrad$_{Si}$ is 6 hours and 20 minutes (1 hour and 35 minutes for each 25% interval).

Beam port #1 Preliminary Calculations.

The neutron flux at the front face of beam port #1 was calculated by using the foil activation technique and the SAND2 neutron spectrum unfolding code. Bare gold, copper, and cobalt wires were irradiated along with gold and copper wires and an aluminum foil covered by 4mm of cadmium for 30 minutes. The wires and cadmium container were taped to the front plate of a test mount mock-up. The reactor was operated at 50kW$_{th}$. Table 4 shows the wire and foil relevant data.

Table 4: Activation data

Wire/foil	mass [mg]	% abund.	AW [gm/mol]	# of TGT Nuclei	Isotope of Interest	Activity [dps]	Half-life [min]	Saturation Activity [dps/nucleus]
Bare								
Au	13.77	100.00	196.9666	4.210E+19	Au-198	6.037E+06	3.881E+03	2.683E-11
Cu	90.7	69.17	62.9296	6.004E+20	Cu-64	1.844E+07	7.621E+02	1.141E-12
Co	24.93	100.00	58.9332	2.547e+20	Co-60	1.548E+04	2.772E+06	8.101E-12
Cd								
Au	10.62	100.00	196.9666	3.247E+19	Au-198	8.259E+05	3.881E+03	4.760E-12
Cu	68.64	69.17	62.9296	4.544E+20	Cu-64	6.076E+05	7.621E+02	4.968E-14
Al	46.52	100.00	26.98154	1.038E+21	Na-24	2.708E+03	8.970E+02	1.138E-16

The saturation activity (decays per second per nucleus) listed in the table above serve as the input into the SANDII neutron unfolding code. The SANDII provides the differential neutron flux (nv cm^{-2} s^{-1}) partitioned into 620 energy groups. Figure 32 shows the resultant neutron spectrum.
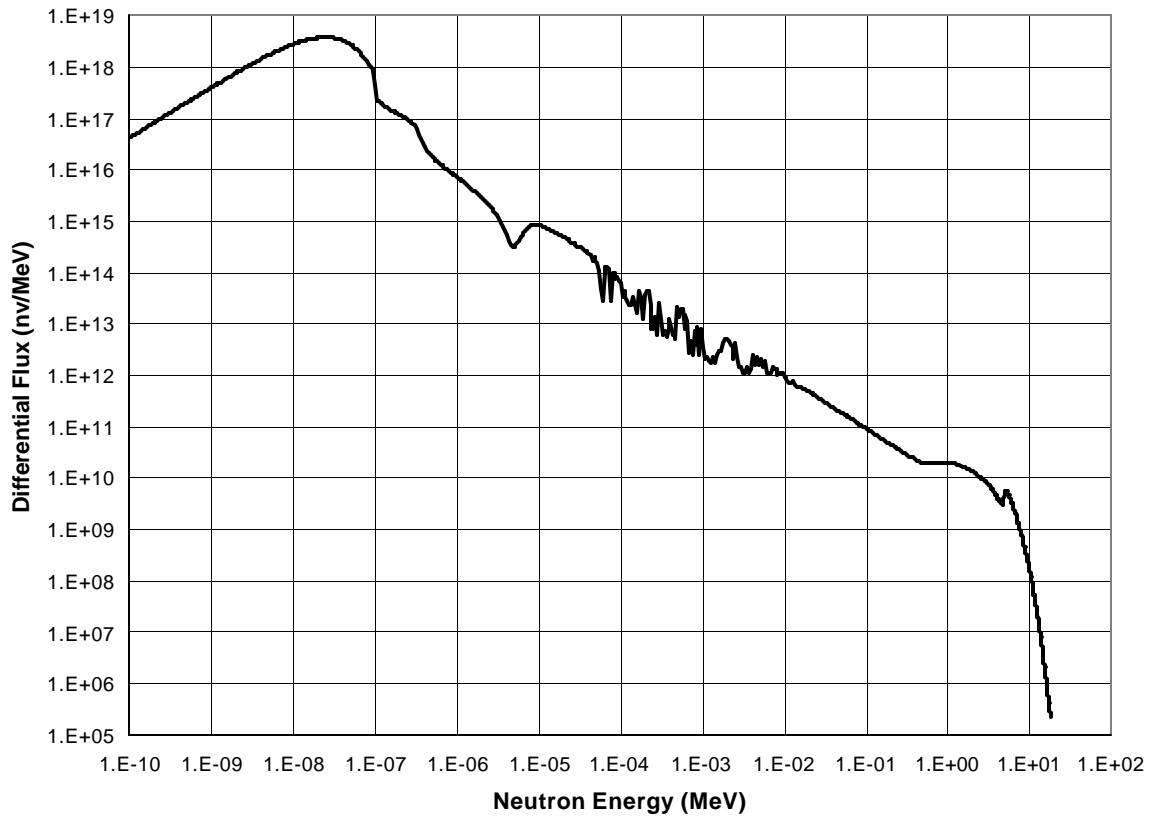

Figure 32: OSURR beam port #1 neutron spectrum

Using the total cross section data file obtained from the LANL nuclear data services web site, the group average total cross sections were calculated using a FORTRAN code in order to best approximate the cross sections in accordance with the energy groupings assigned by the SANDII code.

In general terms, the dose rate is given by the following equation:

$$D_{rate} = \int_0^{E_{max}} \Psi(E) \cdot \Sigma(E) \, dE \tag{25}$$

where $\Psi(E)$ is the energy-dependent flux [nv/cm^{-2} s^{-1}] and $\Sigma(E)$ is the energy-dependent macroscopic cross section [cm^{-1}]. The dose rate given in equation (25) is position and material dependent. In this case, the activation samples were placed on a test mount mock up and pushed to the end of the beam port. By using stopping pins on the test mount, the devices are within one centimeter of the location at which the activation foils and wires were placed. Because the piezoresistive chips are silicon-based, all dose-related calculations are presented in terms of silicon. Given discrete energy groups, equation (25) takes the following form:

$$D_{rate} = \sum_{g=1}^{G} \Psi(E_g) \cdot \Sigma(E_g) \cdot \Delta E_g \tag{26}$$

where the integral has been replaced by the summation (across all energy groups) of the product of the group average differential flux and the group average total cross section multiplied by the group width in energy space. The group average macroscopic cross

section is found by multiplying the group average microscopic cross section by the number of nuclei per unit volume (number density).

$$\Sigma\left(E_g\right) = N \cdot \sigma\left(E_g\right) \tag{27}$$

where N is the number of number density [cm^{-3}] and σ(E) is the energy-dependent microscopic cross section [cm^2].

The purpose of the FORTRAN dose rate code is to ensure that the appropriate weight is given to resonance peaks in the cross section calculations. As can be seen in Figure, assigning a cross section to an energy group, which happened to overlap a resonance peak, would artificially increase the calculated dose rate. Therefore, the FORTRAN code used integrates the cross section data in each energy group and divides by that group's average energy in order to estimate the group average microscopic cross sections. Then, by employing Equations (26) and (27) the total dose rate can be calculated. The calculated neutron spectrum at beam port #1 results in a dose rate of 1.27 Mrad$_{Si}$ hr^{-1}.

The dose rate calculations as outlined above correspond to a reactor power level of 50kW$_{th}$, the power level at which the activated samples were irradiated. Because the dose rate varies linearly with the power level, the dose rate can be calculated for any power rating by dividing by a factor of 50kW. This results in a power dependent dose rate of 25.31Krad$_{Si}$ hr^{-1} kW^{-1}.

In order to take the ramp up to operating power into account, the rise in reactor power as a function of time is approximated by the following equation:

$$P(t) = P_O \cdot e^{\frac{t}{\tau}} \tag{28}$$

where P_o is the reactor power at start up (nominally 0.01 watt), and τ is the reactor period (here 30 seconds). Equation (28) can be solved for the time needed to achieve a specified power level.

$$t = \tau \cdot \ln\left(\frac{P_{max}}{P_o}\right) \tag{29}$$

The drop in reactor power when shutting the reactor down can be approximated by a step function.[27] This results in the time dependent, total dose equations, which are described by the reactor power:

$$D_{ramp} = \int_{0 \cdot min}^{\tau \cdot \ln\left(\frac{P_{max}}{P_o}\right)} D_{rate} \cdot P(t) \, dt \tag{30}$$

$$D_{ss} = \int_{\tau \cdot \ln\left(\frac{P_{max}}{P_o}\right)}^{\tau \cdot \ln\left(\frac{P_{max}}{P_o}\right) + t_{ss}} D_{rate} \cdot P(t) \, dt \tag{31}$$

$$D_{total} = D_{ramp} + D_{ss} \tag{32}$$

where D_{ramp} is the dose delivered during the ramp up to operating power and D_{ss} is the dose delivered during steady state at P_{max}. By fixing the steady state reactor operating power at $50kW_{th}$ and integrating equation (30), the time needed to achieve 1 $Mrad_{Si}$ can be calculated by subtracting the dose received during the initial ramp (20.3 $Krad_{Si}$) from 1 $Mrad_{Si}$ and dividing by the dose rate:

$$t_{ss} = \frac{1 \cdot Mrad_{Si} - D_{ramp}}{D_{rate}} \qquad (33)$$

As a check, the calculated t_{ss} (46.9 min) can be substituted in equation (31). This results in a steady state dose of 979.7 $Krad_{Si}$. When added to the dose obtained during the ramp, the desired 1$Mrad_{Si}$ is obtained.

Appendix B. Measurement System Characterization

Optoisolator Characterization

The 4N37 optoisolator consists of a gallium arsenide infrared emitting diode coupled with a NPN phototransistor packaged in a standard 6-pin DIP. Key operating parameters for the 4N37 optoisolator are given in the following table:

Table 5: Optoisolator operating parameters[28]

Parameter	Value
Input LED	
Forward voltage, V_F	1.5 V (max with I_F = 10mA)
Reverse voltage, V_R	6 V (max)
Cont. Forward Current, I_F	60 mA (max)
Output Transistor	
C-E Voltage, V_{CEO}	30 V (max)
C-E Dark Current, I_{CEO}	50 nA (max with V_{CE} = 10V)
Device	
Turn-off time, t_{off}	10μs (max)
Turn-on time, t_{on}	10μs (max)

As previously discussed, the measurement system used in this research incorporated eight optoisolators controlled by a CPU in order to selectively control which device of interest was measured by the Keithly SMU. The input LEDs were individually wired to the eight output pins of the CPU's parallel port. The collector pins were wired in parallel to the voltage-high output terminal on the Keithly. The emitter pins were individually wired to voltage-high terminal on 12 coaxial cable connectors (stations RAD1 – RAD4 were controlled by the same switches as stations AN1 – AN4, the only difference being the physical location of the attached device). The 12 voltage-low coaxial cable terminals were wired in parallel to the voltage-low input terminal on the SMU.

Based on the information given in Table 5, three key questions must be answered in order to interpret measurements relying on currents passing through the optoisolators. First, what is the voltage applied by the CPU to the input LED, V_F? Second, what is the maximum collector current, I_C, capable of being passed with the optoisolator input LEDs powered by the parallel port? Third, what is the magnitude of the leakage current? In order to answer these questions, a series of tests were performed with the switches' emitter terminals hard-wired to the voltage-low terminal on the Keithly.

First, the parallel port output pin voltages were measured in order to determine the magnitude and stability of the output voltage. This information provides a direct indication of the state of the optoisolator as the parallel port output voltage relates directly to the "on-state" of the optoisolator. As shown in Figure 33, small variances exist between the voltage supplied to the optoisolators. However, the variance in the voltage supplied to a particular optoisolator is one percent or less for all eight optoisolators.
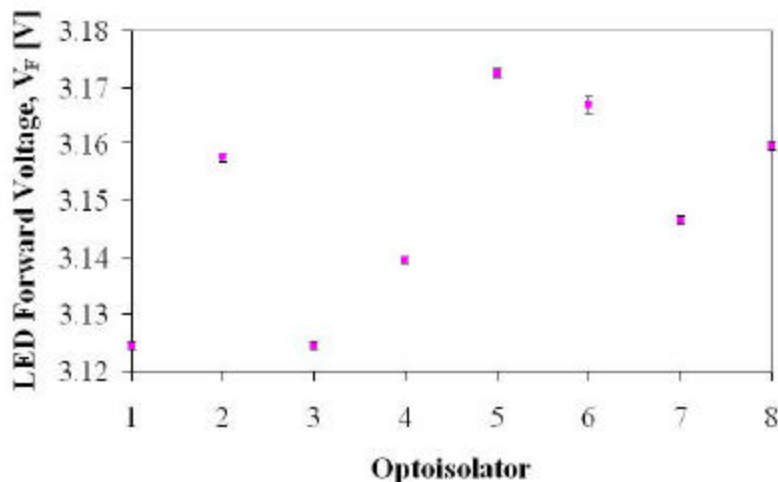

Figure 33: Optoisolator forward voltage [V]

Second, collector-emitter currents, I_{CE}, were measured for each optoisolator with no load applied to the system. This was done in order to determine the maximum passable current. Figure 34 shows the maximum current passed by the optoisolators.
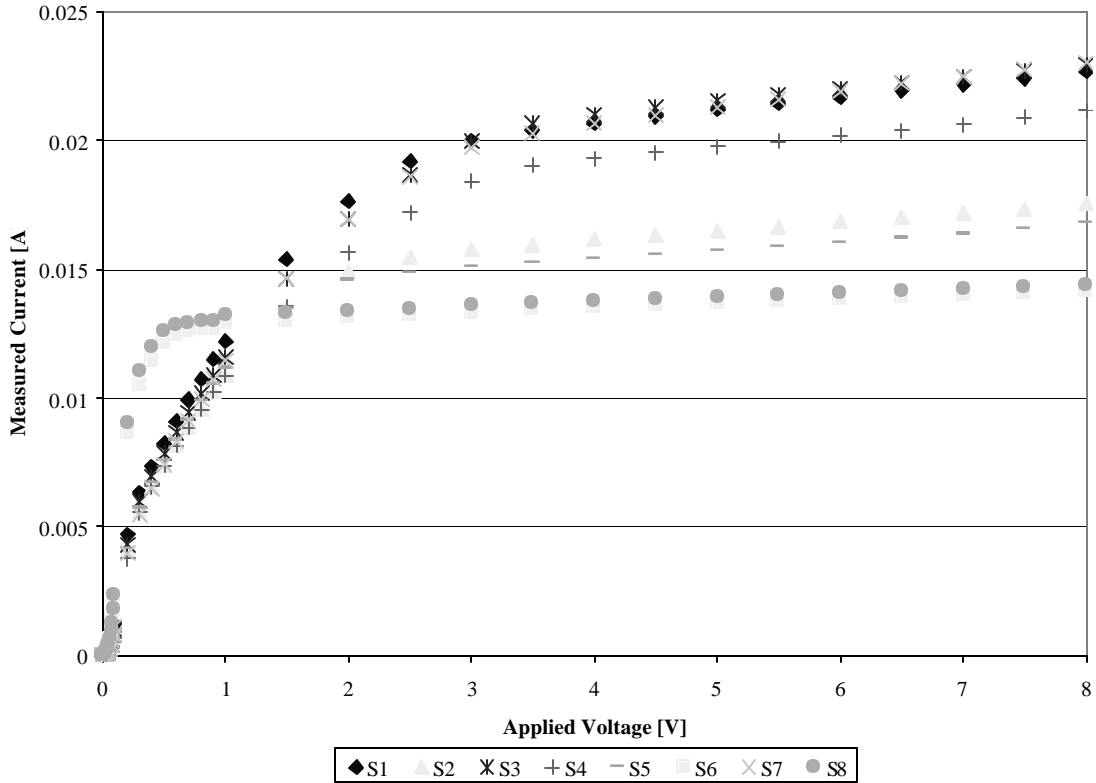

Figure 34: Switch limiting current

The relative error, not shown, in each data point given in Figure 34 is less than one percent in the 0.002V to 8.000V range, but reaches 50 percent at 0.0001V applied voltage. The limiting currents shown in Figure 34 provide an indication of the maximum current the system is capable of measuring (and therefore the minimum resistance). For example, at one volt, the maximum current the system is capable of carrying is on the order of 0.01 amperes. Using Ohm's Law, this corresponds to a resistance of 100 ohms.

Therefore, if the chips were to have a resistance of less than 100 ohms, the resistance of the optoisolators would mask the chips' resistance.

Lastly, because the optoisolators are connected in parallel, it is necessary to determine when the leakage current of an optoisolator in the "off-state" contributes to the measurement of one in the "on-state". Figure 35 shows the switch leakage currents.
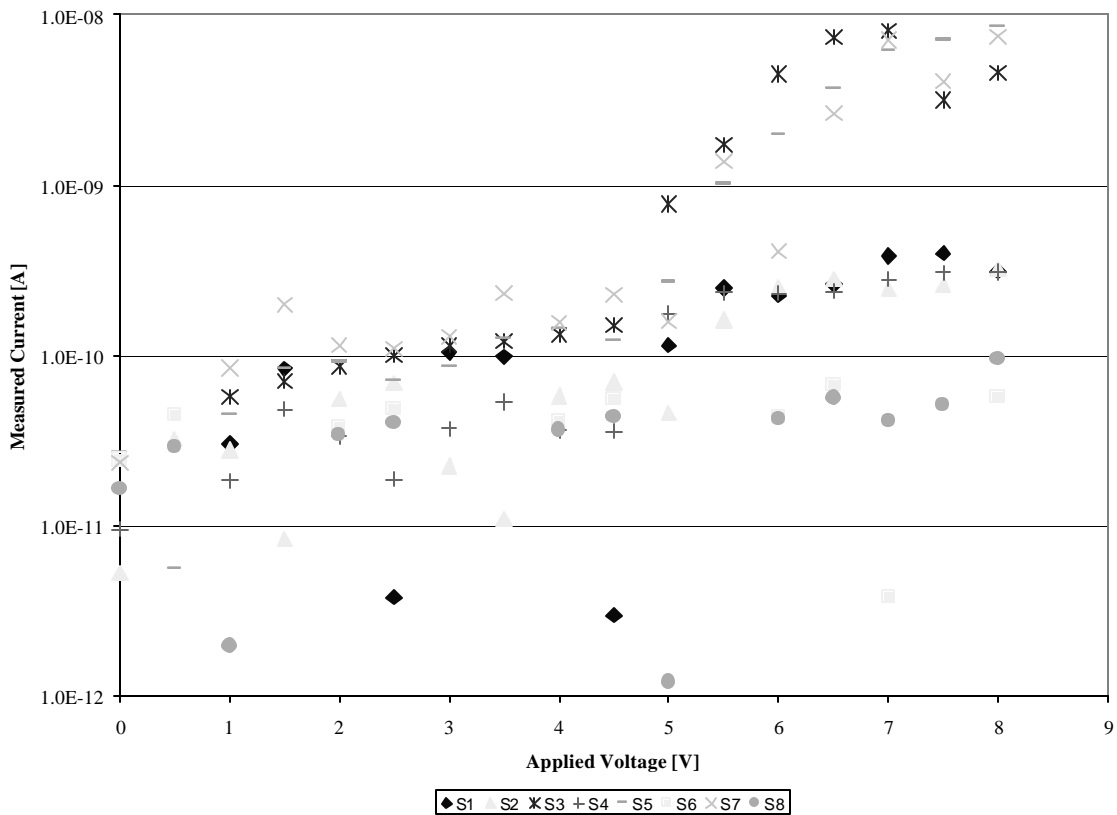

Figure 35: Switch leakage current (semi-log plot)

The relative error in the data in each data point given in Figure 35 is above 100 percent in the 0.0V – 4.5V range and decreases to less then 10 percent with applied voltages greater than six volts. This is because the system noise within the Keithly can appear as currents in the range of tens of picoamperes. The leakage currents evident in

Figure 35 indicate that the optoisolators have an impact only on current measurements below 10 nA and with applied voltages above 5.5V. Again, using Ohm's Law, this corresponds to resistances above 550 MΩ. If the chips were to have a resistance above this level, the leakage currents would mask the true resistance, as more current would be flowing through the switches in the "off state" than the intended chip.

Figure 34 and Figure 35 show some variability in the performance of the optoisolators. While the same manufacturer did not make all eight optoisolators, they all meet the 4N37 specifications. Additionally, it is more likely that the small differences in the voltages sent to the parallel port by the CPU account for the differing "on states" of the optoisolators.

Standard Resistor Characterization

A standard 10kΩ (with a tolerance of 10%) was used to further characterize the measurement system following the characterization of the optoisolators' on- and off-states. A 10kΩ resistor was selected based on initial measurements across the piezoresistive chips. Figure 36 shows the results of the calculated resistance versus the applied voltage. For this system test, the 10kΩ resistor was hard-wired directly to the Keithly SMU.
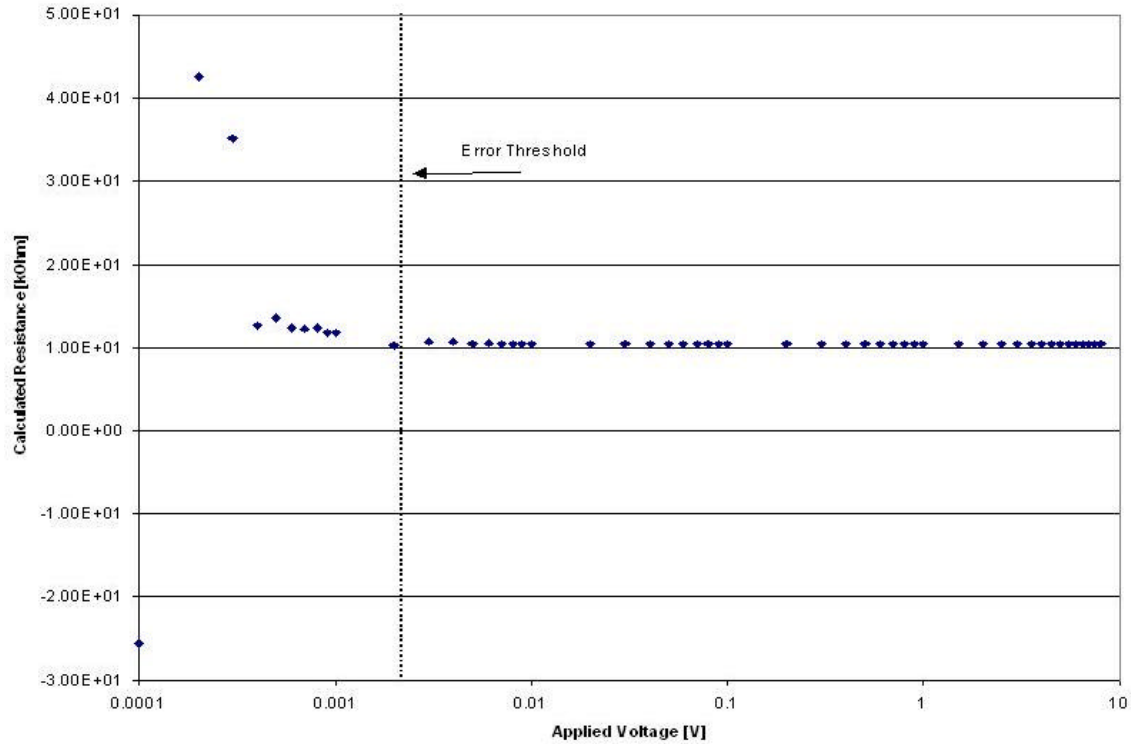
Figure 36: 10kΩ resistor characterization (without switches)

As in the case of the optoisolator characterization, the relative error in the calculated resistance fell below one percent for applied voltages at or above 0.002V. This is the level depicted by the "error threshold" in Figure 36.

For the second characterization test with the 10kΩ resistor, the resistor was hard-wired following the optoisolator emitter terminal to the Keithly. Measurements were taken for each optoisolator switch.

Figure 37: 10KΩ resistor characterization (with switches)

Figure 37 shows the resultant resistance calculations as a function of applied voltage. In this case, the limit for a one-percent relative error was 0.004V. Figure 37 also indicates the 10% tolerance as shown by the upper and lower limit lines.
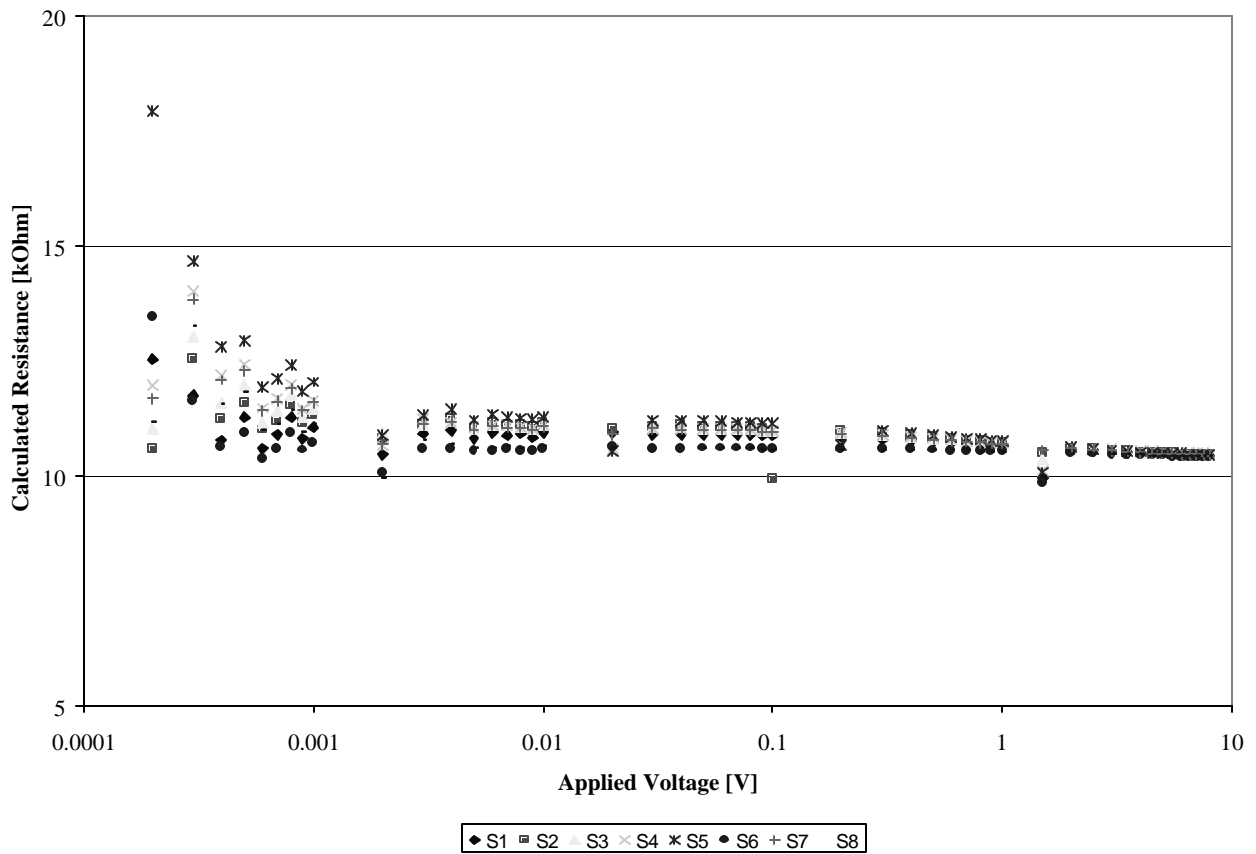
Figure 37: 10KΩ resistor characterization (with switches)

In comparing the results depicted in Figure 36 and Figure 37, an interesting
feature is evident with an applied voltage of 1.5V. At this point, the relative error
increases by two orders of magnitude, to a value of 5%, while on either side of 1.5V, the
relative error is 0.01%. While the error is clearly introduced by the optoisolator, the
exact cause for the increase in the variability of the measurements at this voltage has not
been identified.

Appendix C.   LANL Tests at the Sandia ACRR

Conduct of the Tests

To date, the researchers at LANL have conducted a series of three tests with piezoresistive pressure transducers and accelerometers. These tests were conducted in December 2000, September 2001, and May 2002. During these tests, a variety of transducers were studied in order to determine their suitability for use in studies related to the stockpile stewardship program. In essence, the tests consisted of attaching the devices to a platform that was then lowered into either the FREQ-II or the central cavity of the ACRR. Thermocouples were utilized in order to monitor temperature during the conduct of the tests. No active or passive dosimetry devices were employed during the tests.

Neutron Spectrum Characterization

Researchers at the Sandia ACRR have characterized the reactor's neutron spectrum by employing 44 dosimetry reactions. Some activation foils were covered by cadmium, and in a few cases, the foils were placed in a boron ball. In addition to radiation transport modeling codes, the SAND-II unfolding code was employed.([29]

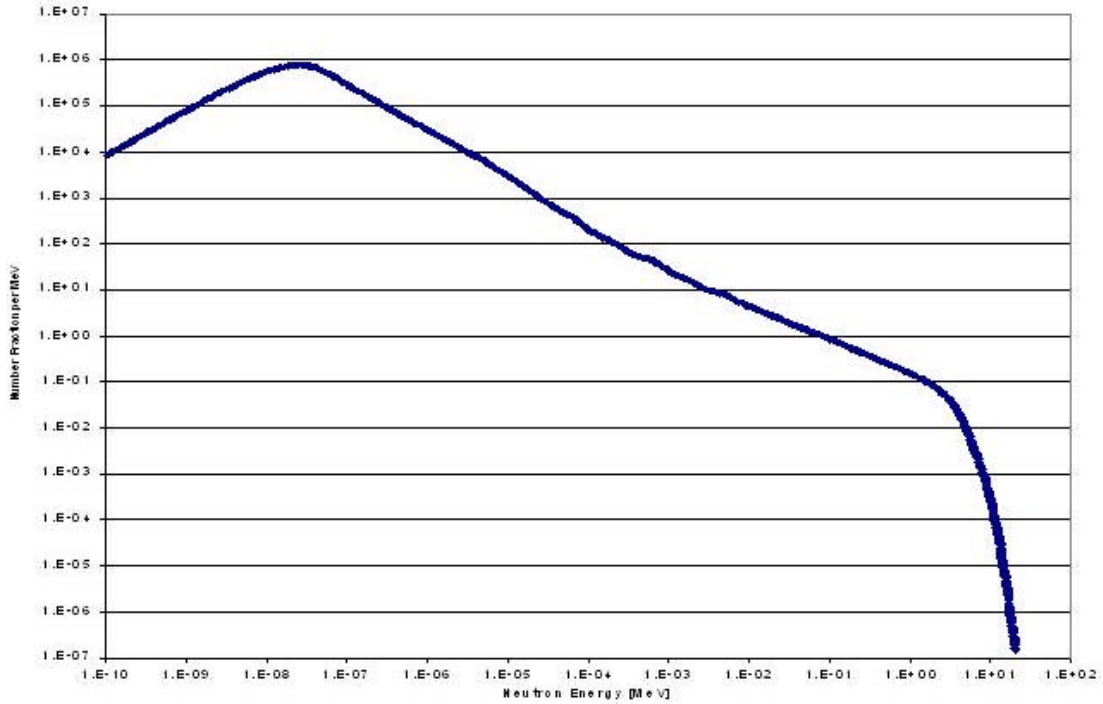Figure 38 shows the resultant relative neutron yield per unit energy [MeV] versus the neutron energy.

Figure 38: Relative neutron yield per MeV vs neutron energy

Test Pulse Shapes

Figure 39 was generated from the data available from the May 2002 tests,
reflecting three of the five runs executed (7540 through 7542). Data analysis shows that
the FWHM of the peak pulse was on the order of 29 ms and that the peak power was on
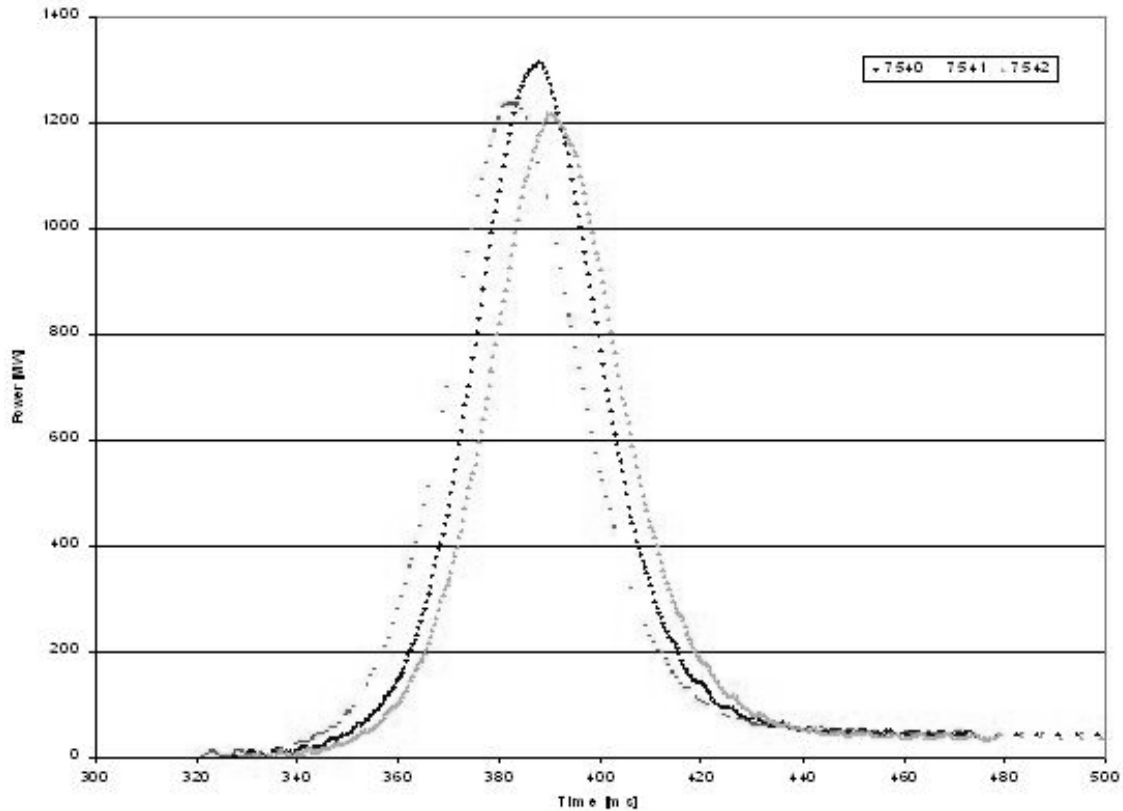the order of 1300MW.

Figure 39: Representative Sandia ACRR pulses (7540-7542)

Estimated Total Dose Delivered

In order to arrive at an estimated dose delivered to the test devices, the energy yield curves were integrated over time, resulting in an average energy yield of 21.87 MJ. By applying a neutron fluence normalization constant $(3.5052 \times 10^{14}$ cm^{-2} at 16.66 MJ$)^{24}$ and dividing by the pulse width (123.2 ms) an estimated total neutron flux of 3.74×10^{15} cm^{-2} s^{-1} is obtained. Then, the standard dn/dE is obtained by multiplying the total flux by the relative neutron yield given in Figure 38 and dividing each group by the average group energy. The gamma dose is treated in a similar fashion, using a gamma dose normalization constant of 197.8 Krad$_{Si}$ at 16.66 MJ.

83

Using the same program used in the preliminary dosimetry calculations in Annex A-3, an estimated neutron dose rate of 170 ± 10 Mrad$_{Si}$ per hour is obtained. This results in a neutron total dose of 5.9 ± 0.4 Krad$_{Si}$ and a gamma total dose of 260 ± 60 Krad$_{Si}$.

Raw Data

Figure 40 shows a representative raw data output file. As this file was produced during the course of the gamma cell irradiation and the thermocouple was not used, no temperature is given. For each chip, seven voltage sweeps were performed with the specified parameters.

```
"PR Diaphragm I-V Measurements"
"12/13/2002    12:18:46"
"V Range: 0 [V] to 8.0 [V]"
"Step size: .50 [V]"
"Temp [V]: "
""

"Voltage[V]","Current[A]"
0,9.875E-08
.5,4.7868E-05
1,9.3716E-05
        1.5,1.4095E-04
2,1.8953E-04
2.5,2.3707E-04
3,2.8706E-04
3.5,3.3619E-04
4,3.8551E-04
4.5,4.3439E-04
5,.0004856
5.5,5.3479E-04
6,5.8624E-04
6.5,6.3794E-04
7,6.7627E-04
7.5,7.3529E-04
```

Figure 40: Representative raw data from output file

Parsed and Conditioned Data

As shown in Figure 41, the parsed and conditioned data files included the following: the time elapsed in minutes, applied voltage in volts, measured current in amperes, and the standard deviation in the measurement, also in amperes. The bottom value in the figure of 999.0 indicates that the thermocouple was not used during this particular measurement.

```
1.129833E+02    0.0000E+00    1.0164E-07    2.3095E-09
1.129833E+02    5.0000E-01    4.9002E-05    5.4346E-07
1.129833E+02    1.0000E+00    9.5971E-05    1.0067E-06
1.129833E+02    1.5000E+00    1.4448E-04    1.5810E-06
1.129833E+02    2.0000E+00    1.9432E-04    2.1392E-06
1.129833E+02    2.5000E+00    2.4379E-04    2.9871E-06
1.129833E+02    3.0000E+00    2.9368E-04    2.9584E-06
1.129833E+02    3.5000E+00    3.4358E-04    3.2997E-06
1.129833E+02    4.0000E+00    3.9355E-04    3.5908E-06
1.129833E+02    4.5000E+00    4.4361E-04    4.1127E-06
1.129833E+02    5.0000E+00    4.9395E-04    3.7622E-06
1.129833E+02    5.5000E+00    5.4428E-04    4.2234E-06
1.129833E+02    6.0000E+00    5.9478E-04    3.8083E-06
1.129833E+02    6.5000E+00    6.4528E-04    3.2866E-06
1.129833E+02    7.0000E+00    6.9388E-04    7.7961E-06
1.129833E+02    7.5000E+00    7.4548E-04    4.5449E-06
1.129833E+02    8.0000E+00    7.9761E-04    1.3964E-06

999.000000000000
```

Figure 41: Representative parsed and conditioned data

Representative Mathcad^{TM} File

Figure 42 shows a portion of a representative Mathcad data manipulation file. As shown in the figure, each measured current data point is first divided by the applied voltage at which that measurement was taken in order to obtain the resistance. The initial resistance as that voltage is then subtracted in order to obtain the difference. The change in resistivity is then computed by dividing by the initial resistivity.

data1 :=
[disk icon]
C:\P10b.dat

data2 :=
[disk icon]
C:\P9a.dat

data3 :=
[disk icon]
C:\P8a.dat

$l := rows(data1)$

$l = 1.866 \times 10^3$

$n := 0, 1 .. 1524$ $m := 0 .. 9$

$l2 := rows(data2)$

$n2 := 0, 1 .. l2 - 1$

$l3 := rows(data3)$

$+$

$n3 := 0, 1 .. l3 - 1$

$x1_n := data1_{n,1}$

$x2_{n2} := data2_{n2,1}$ $t2_{n2} := data2_{n2,0}$ $x3_{n3} := data3_{n3,1}$ $t3_{n3} := data3_{n3,0}$

$t1_n := data1_{n,0}$

$$y1_n := if\left(data1_{n,1} = 0, \frac{data1_{n,1}}{data1_{n,2}} - \frac{data1_{0,1}}{data1_{0,2}}, if\left(data1_{n,1} = 0.5, \frac{data1_{n,1}}{data1_{n,2}} - \frac{data1_{1,1}}{data1_{1,2}}, if\left(data1_{n,1} = 1, \frac{data1_{n,1}}{data1_{n,2}} - \frac{data1_{2,1}}{data1_{2,2}}, if\left(data1_{n,1}\right.\right.\right.$$

$$y1_{n7+l-1} := if\left(data7_{n7,1} = 0, \frac{data7_{n7,1}}{data7_{n7,2}} - \frac{data1_{0,1}}{data1_{0,2}}, if\left(data7_{n7,1} = 0.5, \frac{data7_{n7,1}}{data7_{n7,2}} - \frac{data1_{1,1}}{data1_{1,2}}, if\left(data7_{n7,1} = 1, \frac{data7_{n7,1}}{data7_{n7,2}} - \frac{data1_{2,1}}{data1_{2,2}}, if\right.\right.\right.$$

Figure 42: Representative Mathcad^{TM} data manipulation file

Bibliography

[1] McCready, S. and T. Harlow, A. Heger, and K. Holbert. "Piezoresistive Micromechanical Transducer Operation in a Pulsed Neutron and Gamma Ray Environment." Unpublished paper submitted to the IEEE Nuclear and Space Radiation Effects Conference, July 2002.

[2] Bridgman, P.W. "The Effect of Homogeneous Mechanical Stress on the Electrical Resistance of Crystals." Physical Review, Vol. 42, 15 December 1932.

[3] Pfann, W.G. and R.N. Thurnston. "Semiconducting Stress Transducers Utilizing the Transverse and Shear Piezoresistance Effects." Journal of Applied Physics. Vol. 32, No. 10. October, 1961.

[4] Smith, Charles S. "Piezoresistance Effect in Germanium and Silicon." Physical Review, Vol. 94. No 1, 1 April, 1954.

[5] Mahan, Gerald D. *Many-Particle Physics* (2nd Edition). New York: Plenum Press, 1990.

[6] Tandeske, Duane. *Pressure Sensors:Selection and Application*. New York: Marcel Dekker, Inc., 1991.

[7] Patrick L. Walter. "Dynamic Force, Pressure, & Acceleration Measurement (Part 2)" Paper submitted to the Measurements and Controls Journal and provided on the Internet, http://www.endevco.com/main/literature/tutorials.html, June 1999.

[8] Knudson, A.R. (et al). "The Effects of Radiation on MEMS Accelerometers." IEEE Trans. Nucl. Sci. NS-43 3122 (1996).

[9] Sze, S.E. *Physics of Semiconductor Devices* (2nd Edition). New York: John Wiley and Sons, 1981.

[10] van Lint, V.A.J. *Mechanisms of Radiation Effects in Electronic Materials, Volume 1*. New York: John Wiley and Sons, 1980.

[11] Yu, Z. (et al). *PISCES-2ET and its Application Subsystems*. Stanford: Stanford University, 1994.

[12] Kraus, John D. and Daniel A. Fleisch. *Electromagnetics with Applications* (5th Ed.). Boston: McGraw-Hill, 1999.

[13] Ma, T.P. and Paul V. Dressendorfer. *Ionizing Radiation Effects in MOS Devices and Circuits.* New York: John Wiley and Sons, 1989.

[14] Messenger, George C. "A Summary Review of Displacement Damage from High Energy Radiation in Silicon Semiconductors and Semiconductor Devices." IEEE Trans. Nucl. Sci. NS 39-469 (1992).

[15] Werner, Matthias R. and Wolfgang R. Fahrner. "Review on Materials, Micro-sensors, Systems, and Devices for High-Temperature and Harsh-Environment Applications." IEEE Trans. Nucl. Sci., NS-48, 249(2001).

[16] Knudson, A.R. (et al). "The Effects of Radiation on MEMS Accelerometers." IEEE Trans. Nucl. Sci. NS-43 3122 (1996).

[17] Padgaonkar, Swarupa (et al). "Comparison of 14 MeV neutron-induced and 1 MeVelectron-induced radiation damage in crystalline silicon." J. Phys.D: Appl. Phys. Vol. 24 (1991).

[18] Lee, C.I (et al). "Total Dose Effects on Micro-mechanical Systems (MEMS): Accelerometers." IEEE Trans. Nucl. Sci., NS-43 3127 (1996)

[19] Janesick, James (et al). "Radiation Damage in Scientific Charge-Coupled Devices." IEEE Trans. Nucl. Sci., NS-36 572 (1989).

[20] Messenger, George C. and Milton S. Ash. *The Effects of Radiation on Electronic Systems* (2nd Edition). New York: Van Nostrand Reinhold, 1992.

[21] Mottet, S. and A. Riozès. "Defect formation kinetics in irradiated silicon at 300K," in *Defects and Radiation Effects in Semiconductors, 1978*. Ed. J.H. Albany. Bristol, U.K.: The Institute of Physics, 1979.

[22] Gover, James E. Course handout, IEEE Nuclear and Space Radiation Effects Conference Short Course, Colorado Springs, July 1984.

[23] Taylor, John R. *An Introduction to Error Analysis: The Study of Uncertainties in Error Analysis.* Mill Valley: University Science Press, 1982.

[24] Griffin, Patrick, Research Associate, Sandia National Laboratories, Albuquerque, NM. Personal Correspondence, December 2002.

[25] Kulite Semiconductor Products Inc. "XTE-190(M) Series and XTEL-190(M) Series." Extract from product data sheet provided on the Internet. http://216.197.110.63/pdfs/pdf_Data_Sheets/XTE.XTEL-190.pdf, December 2002.

[26] Endevco Corp."Model 7264B." Extract from product data sheet provided on the Internet. http://www.endevco.com/data-sheets/72xx/7264B-500-2000.pdf, December 2002.

[27] Talnagi, J. Senior Research Associate, Ohio State University Research Reactor Facility, Columbus OH. Personal Correspondence. November 2002.

[28] NTE Electronics Inc. "NTE3041 Optoisolator NPN Transistor Output." Extract from product data sheet provided on the Internet. http://www.nteinc.com/specs/3000to3099/pdf/nte3041.pdf September 2002.

[29] Griffin, Patrick and others. "Characterization of ACRR Reference Benchmark Field." Unpublished. December 2002.

Vita

Captain Samuel J. Willmon graduated from the United States Military Academy at West Point, New York in 1994 with a Bachelor of Science degree in Physics. Following his commissioning as a second lieutenant of Infantry, he was assigned to 1st Battalion, 15th Infantry in Schweinfurt, Germany. While in Germany, he served as a rifle platoon leader, mortar platoon leader, headquarters and headquarters company executive officer, and battalion maintenance officer. During his tour in Germany, he spent six months with Task Force 1-26, the Blue Spaders, in Bosnia-Herzogovina as part of IFOR, CFOR, and later SFOR.

Following the Infantry Captain's Career Course at Fort Benning, Georgia in 1999, Captain Willmon was assigned as the assistant brigade operations officer for the 1st Brigade, 2nd Infantry Division at Camp Casey, Korea. After ten months on brigade staff, Captain Willmon assumed command of A Company, 2nd Battalion, 9th Infantry, also at Camp Casey. In September 2001, he entered the Graduate School of Engineering at the Air Force Institute of Technology at Wright-Patterson Air Force Base, Ohio. Upon graduation, he will be assigned to the National Ground Intelligence Center.

1. REPORT DATE *(DD-MM-YYYY)* 25-03-2003	2. REPORT TYPE **Master's Thesis**	3. DATES COVERED *(From – To)* Jun 2002 – Mar 2003

4. TITLE AND SUBTITLE	
TOTAL DOSE EFFECTS OF IONIZING AND NON-IONIZING RADIATION ON PIEZORESISTIVE PRESSURE TRANSDUCER CHIPS	5a. CONTRACT NUMBER
	5b. GRANT NUMBER
	5c. PROGRAM ELEMENT NUMBER

6. AUTHOR(S)	
Willmon, Samuel J., Captain, USA	5d. PROJECT NUMBER ENP03-281
	5e. TASK NUMBER
	5f. WORK UNIT NUMBER

7. PERFORMING ORGANIZATION NAMES(S) AND ADDRESS(S) Air Force Institute of Technology Graduate School of Engineering and Management (AFIT/EN) 2950 P Street, Building 640 WPAFB OH 45433-7765	8. PERFORMING ORGANIZATION REPORT NUMBER AFIT/GNE/ENP/03-11

9. SPONSORING/MONITORING AGENCY NAME(S) AND ADDRESS(ES) DTRA/CSNP Attn: Mr. Jerry Baird 2801 Telegraph Rd Alexandria, VA 22310 (703) 625-8128	10. SPONSOR/MONITOR'S ACRONYM(S)
	11. SPONSOR/MONITOR'S REPORT NUMBER(S)

12. DISTRIBUTION/AVAILABILITY STATEMENT

APPROVED FOR PUBLIC RELEASE; DISTRIBUTION UNLIMITED.

13. SUPPLEMENTARY NOTES

14. ABSTRACT

The effects of ionizing and non-ionizing radiation on the resistivity of silicon-based, piezoresistive bulk micro-machined chips from pressure transducers were examined. Standard current-voltage (I-V) measurements were taken in-situ and post-irradiation during isothermal annealing at room temperature. One group of chips was irradiated to a maximum total gamma dose of $1 Mrad_{Si}$ in the 11,000 Ci ^{60}Co gamma cell at Ohio State University. The second group of chips was irradiated at the Ohio State University Research Reactor facility to a maximum total neutron dose of 4 $Mrad_{Si}$ using beam port #1.

The resistivity was shown to decrease during gamma irradiation as a result of Compton current generation and increase during neutron irradiation as a result of displacement damage. During irradiation in the gamma cell, the chips exhibited a 0.45 ± 0.19 % decrease in resistivity at saturation. During the neutron and gamma irradiation in the reactor, the chips exhibited a peak change in resistivity of 2.503 ± 0.003% at 2 $Mrad_{Si}$, 3.055 ± 0.002% at 3 $Mrad_{Si}$, and 3.6921% (with unknown uncertainty) at 4 $Mrad_{Si}$. Regardless of the total dose received, all chips demonstrated a permanent change in resistivity of 0.7697 ± 0.0006% at room temperature.

15. SUBJECT TERMS
Piezoresistive, Transducer, Radiation, Damage mechanism

16. SECURITY CLASSIFICATION OF:			17. LIMITATION OF ABSTRACT	18. NUMBER OF PAGES	19a. NAME OF RESPONSIBLE PERSON James C. Petrosky, LTC, USA (ENP)
a. REPORT U	b. ABSTRACT U	c. THIS PAGE U	UU	103	19b. TELEPHONE NUMBER *(Include area code)* (937) 255-6565, ext 4600; e-mail: James.Petrosky@afit.edu